ФИЗИКА ЭЛЕМЕНТАРНЫХ ЧАСТИЦ И АТОМНОГО ЯДРА
2016. Т. 47. ВЫП. 1

RADIOACTIVE NUCLEAR BEAMS OF COMBAS FACILITY

A. G. Artukh [1,*], *S. A. Klygin* [1], *G. A. Kononenko* [1],
D. A. Kyslukha [1,2], *S. M. Lukyanov* [1], *T. I. Mikhailova* [1],
Yu. Ts. Oganessian [1], *Yu. E. Penionzhkevich* [1], *Yu. M. Sereda* [1],
A. N. Vorontsov [1,3], *B. Erdemchimeg* [1,4]

[1] Joint Institute for Nuclear Research, Dubna
[2] V. N. Karazin Kharkiv National University, Kharkiv, Ukraine
[3] Institute for Nuclear Research, Kyiv
[4] National University of Mongolia, Nuclear Research Center, Ulaanbaatar

---

[*] E-mail: artukh@jinr.ru

ФИЗИКА ЭЛЕМЕНТАРНЫХ ЧАСТИЦ И АТОМНОГО ЯДРА
2016. Т. 47. ВЫП. 1

RADIOACTIVE NUCLEAR BEAMS OF COMBAS FACILITY

A. G. Artukh [1,*], *S. A. Klygin* [1], *G. A. Kononenko* [1],
D. A. Kyslukha [1,2], *S. M. Lukyanov* [1], *T. I. Mikhailova* [1],
Yu. Ts. Oganessian [1], *Yu. E. Penionzhkevich* [1], *Yu. M. Sereda* [1],
A. N. Vorontsov [1,3], *B. Erdemchimeg* [1,4]

[1] Joint Institute for Nuclear Research, Dubna
[2] V. N. Karazin Kharkiv National University, Kharkiv, Ukraine
[3] Institute for Nuclear Research, Kyiv
[4] National University of Mongolia, Nuclear Research Center, Ulaanbaatar

The basic ion-optical characteristics of the high-luminosity and high-resolution kinematic separator COMBAS, realized for the first time on the strong focusing principle, are presented. The developed facility allows one to separate the high-intensity secondary radioactive beams in a wide range of mass numbers A and atomic numbers Z, which are produced in heavy-ion reactions in the energy range of $20 \leqslant E \leqslant 100$ MeV/A (Fermi energy domain). Two distinct detector systems, such as realized Si strip-detector telescope and the three-dimensional time-projection chamber of promising development, are discussed. A program of the investigations of nuclear reaction mechanisms at intermediate energies of 20–100 MeV/A, measurement of the radii of unstable nuclei, study of the cluster structure of light nuclei near the nuclear drip-line, and search for ^{26,28}O resonances in exchange reactions is proposed. The upgrading of experimental facility by the integration of COMBAS separator with the ion catcher is discussed.

Представлены базисные ионно-оптические характеристики светосильного и высокоразрешающего кинематического сепаратора COMBAS, который реализован впервые в мире на основе принципов жесткой фокусировки. Созданная установка позволяет сепарировать высокоинтенсивные вторичные пучки радиоактивных ядер в широком диапазоне массовых чисел A и атомных номеров Z, которые получаются в реакциях с тяжелыми ионами в области энергий $20 < E < 100$ МэВ/A (область ферми-энергии). Обсуждаются два различных типа детектирующих систем: реализованный телескоп из кремниевых стриповых детекторов и разрабатываемая трехмерная времяпроекционная камера. Предлагается научная программа исследований механизмов ядерных реакций при промежуточных энергиях в диапазоне 20–100 МэВ/A, включающая измерение

---

[*] E-mail: artukh@jinr.ru

радиусов нестабильных ядер, изучение кластерной структуры легких ядер вблизи границ ядерной стабильности, а также поиск резонансов в нестабильных ядрах ^{26,28}O в обменных реакциях. Обсуждаются планы усовершенствования экспериментального комплекса с помощью объединения сепаратора COMBAS с ионной ловушкой.

PACS: 25.60.-t; 25.70.-z

INTRODUCTION

An extremely wide variety of heavy-ion reactions involving an enormous number of possible projectile and target nuclei combinations opens favorable prospects for obtaining yet unknown isotopes of known elements, isotopes featuring a large excess or deficit of neutrons and situated in the vicinity of or even beyond the nucleon drip-line. The choice of reaction characterized by the largest cross section for the production of the objects of interest is very important for obtaining the maximum yield of rare exotic nuclei.

Secondary beams of radioactive nuclei obtained in exchange and fragmentation reactions with the wide momentum and angular distributions are known to possess a number of drawbacks if they are separated and formed using only the in-flight separation technique [1–5]. The most important problem is difficulty in obtaining single isotopic and monochromatic beam, owing to a wide range of isotopic compositions with different atomic numbers Z and mass numbers A, as well as their ions in different charge states.

To identify unambiguously the nuclear-reaction products over A and Z, it is necessary not only to measure the magnetic rigidity $B\rho$ of the separator

$$B\rho \sim \frac{P}{Q} = \frac{AV}{(Z-N)}, \tag{1}$$

but also to apply the multiparametric registration technique using multidetector system

$$\Delta E \sim \left(\frac{Z}{V}\right)^2, \quad \Delta E + E_r \sim \frac{(AV^2)}{2}, \quad \text{TOF} \sim \left(\frac{1}{V}\right). \tag{2}$$

Here A, Z are the mass and atomic numbers of nuclei; $(Z-N)$ is the charge state of ions with N — electron number, V — projectile velocity, ΔE — projectile energy loss in the thin penetrating detector, E_r — residual energy measurement in thick detector, TOF — time-of-flight particle.

The COMBAS experimental facility (Fig. 1) is intended to perform the following tasks:

(i) studying the mechanisms of nuclear reactions with heavy ions in the energy range of $20 \leqslant E \leqslant 100$ MeV/A (Fermi energy domain) with the aim of using the results of this study in obtaining secondary beams of radioactive nuclei;

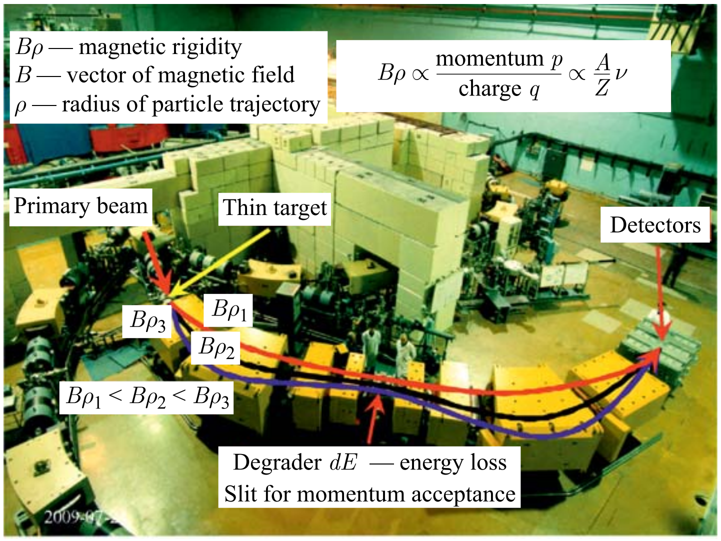

Fig. 1. General view of the COMBAS kinematic separator installed in the experimental hall of the U400M cyclotron of the FLNR at the JINR

ii) studying the structure of neutron- and proton-rich isotopes of light and medium elements;

(iii) studying mechanisms of nuclear reactions with single-isotope and monochromatic beams of radioactive nuclei, including fusion reactions for synthesis of neutron-rich isotopes of heavy and superheavy elements.

1. STRUCTURE OF THE COMBAS FACILITY

The experimental facility consists of three functional parts [5–7] (Fig. 2):

(i) the high-luminosity COMBAS kinematic separator F_0–F_{a1} for obtaining and forming secondary beams of radioactive nuclei, as well as for transporting these beams to exit achromatic focus F_{a1};

(ii) the section F_{a1}–F_{a2} for ion-optical matching of the output emittance of the COMBAS kinematic separator with the input aperture of the detector system. The section is equipped with the quadrupole triplet and two coordinate profilometers which operate also as track detectors to determine the coordinates of the projectiles on the target and angular beam divergence;

(iii) the detector complex with multiparametric electronic system to identify unambiguously over A and Z both of light nuclei (long-range particles) and of heavy ones (short-range particles).

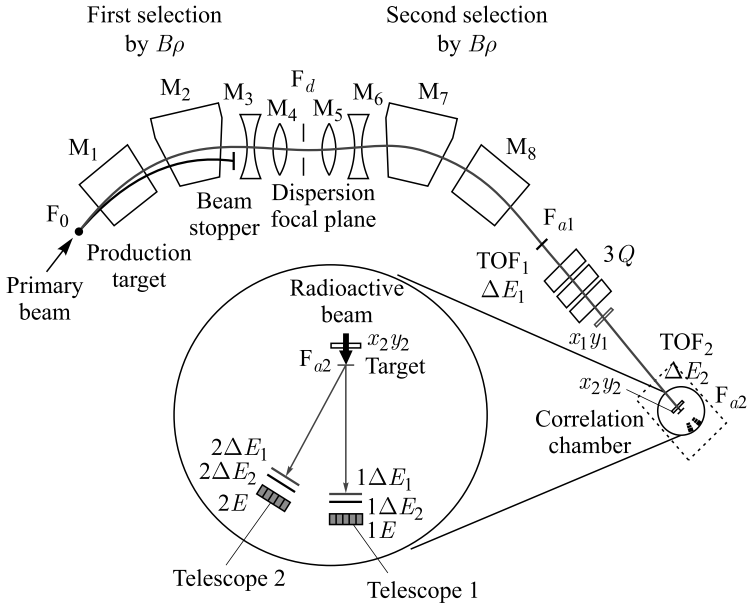

Fig. 2. Diagram of the experimental setup based on the COMBAS kinematic separator: F_0–F_{a1} — magneto-optical system of the COMBAS separator; F_{a1}–F_{a2} — section of ion-optical matching of the COMBAS separator output emittance with the detector complex, which is equipped with quadrupole triplet $3Q$ with diagnostic detectors; M_1–M_8 — multipole magnets; TOF_1, TOF_2 — time-of-flight counters; F_d — dispersion focus; F_a — achromatic focus

1.1. COMBAS Kinematic Separator. For the collection efficiency of short-lived nuclei produced by exchange and fragmentation reactions in the collision of the stable projectile with target nucleus at energies around 20–100 MeV$/A$ with the wide momentum and angular distributions, the ion-optical scheme of the COMBAS kinematic separator was fulfilled on the principles of strong focusing [6, 7] for the first time. The magnetic structure of the COMBAS separator (F_0–F_{a1} in Fig. 2) is formed by the cascade of wide-aperture multipole magnets M_1–M_8, in which quadrupole, sextupole, and octupole components necessary for minimizing aberrations of the first, second, and third orders, are generated using the pole piece profiling method. The use of wide aperture multipole magnets made it possible to obviate the need of isolated quadrupole, sextupole, and octupole lenses which apertures limit the aperture of the separating channel.

The COMBAS separating channel is composed of eight multipole magnets M_1–M_8 which form the wide aperture separator with triple focusing of particles at the final focus F_{a1} (by the energy, along the horizontal and vertical axes).

The separator configuration is composed of two identical sections M_1–M_4 and M_5–M_8 with the plane of symmetry in the middle (dispersion focus F_d). The first analyzing section M_1–M_4 acts as the filter of high-energy particles by their momentum with the rejection of the primary beam, and the second section M_5–M_8 compensates for the dispersion of the first section and minimizes the aberration effects at final achromatic focus F_{a1}. Dispersion function $D(S)$ is shown by the solid line in Fig. 3. From the figure it follows that function $D(S)$ has a zero derivative in the middle of the separator at the position of intermediate focus F_d. This behavior of dispersion function $D(S)$ ensures mirror symmetry of both separator parts, which is necessary for obtaining the achromatism of transported particles at final focus F_a. Moreover, this shape of the dispersion

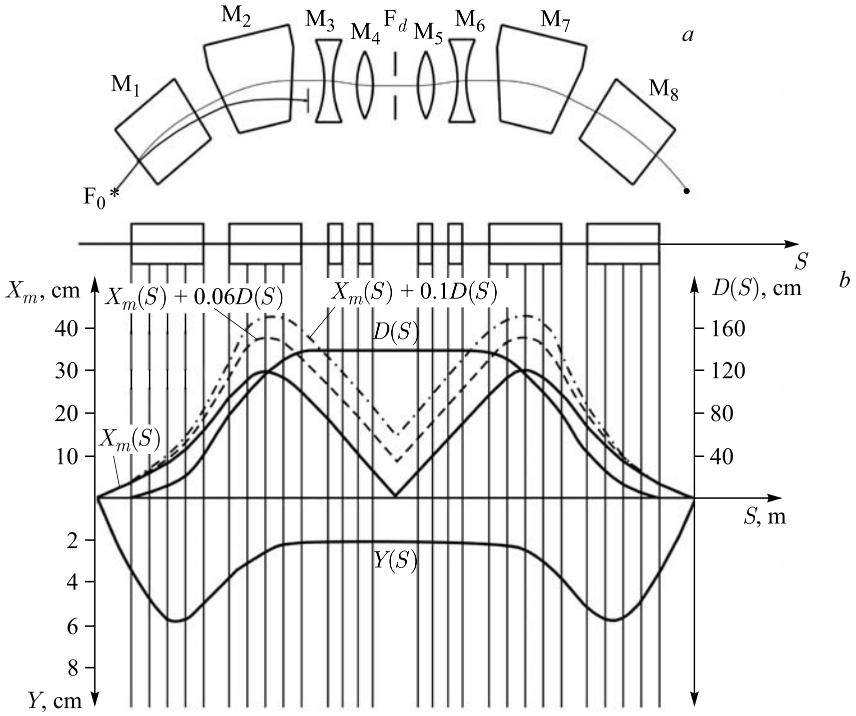

Fig. 3. Magneto-optical system of the COMBAS separating channel: *a*) diagram of the separator's magnetic structure; *b*) ion-optical scheme (coordinate grid) with particle beam envelopes in median plane X_m for three variants of the momentum acceptance. $X_m(S)$ is the particle beam envelope with zero momentum divergence (i.e., for monochromatic particles), $X_m(S) + 0.1D(S)$ is the envelope at ±10% momentum acceptance, $X_m(S) + 0.06D(S)$ is the envelope at ±6% momentum acceptance, and $D(S)$ is the dispersion function

function allows degrader D to be used at intermediate focus F_d without distorting the achromatism of particle focusing at final focus F_a. The coordinate part of Fig. 3 shows the behavior of the beam envelope function in median plane X_m for three values of particle momentum acceptance: $\Delta p/p = 0\%$ $(X_m(S))$, $\pm 6\%$ $(X_m(S) + 0.06D(S))$, and $\pm 10\%$ $(X_m(S) + 0.1D(S))$, as well as in vertical plane Y along the separator path — $Y(S)$. The applicability of penetrating foil D (the degrader) at the position of the maximum dispersion F_d helps to radically improve isotope separation by the second section owing to the difference of the energy losses in the degrader foil between the separated and satellite products of nuclear reactions. In addition, the flight base of the second section in which the intense beam of primary particles is absent can be effectively used for time-of-flight measurements, which are necessary for isotope identification by the mass number in some questionable cases (due to the overlap of wide momentum distributions of separated nuclides and the contributions of different charge states of these nuclides). The separation rate is determined by the time of flight of the full magnetic channel base (from tens to hundreds of nanoseconds).

In the configuration performed thereby, the high luminosity COMBAS kinematic separator provides particle separation simultaneously by momentum p, specific energy loss $\Delta E/\Delta X$ (the degrader), and time of flight TOF. This provides the means for obtaining the high selectivity of nuclides by the mass number A and the atomic number Z with acceptable elimination of the background of primary beam particles (projectiles). Thin penetrating avalanche counters (or thin scintillators) are used as start–stop time-of-flight detectors in TOF measurements. Marked in Fig. 2 with avalanche counters TOF_1 in F_{a1} and TOF_2 in F_{a2}, the start–stop base determines the time-of-fight interval for TOF.

The kinematic separator parameter of utmost importance that satisfies the requirements of the maximum collection efficiency of exchange and fragmentation reactions is the value of its momentum acceptance. Figure 4 presents the view of the dispersion plane F_d of the COMBAS kinematic separator, which was recorded by a video camera in the experiment on the ^{11}B beams with an energy of 33 MeV/A. The cascade of light vertical bands 1–15 on the coordinate grid of the luminophor platform was obtained by ionizing the luminophor with the primary monochromatic ^{11}B beam. In this case, magnetic rigidity $\Delta B\rho/B\rho$ was changed by the first section M_1–M_4 with step $\Delta B\rho/B\rho = 1\%$ (or in momentum space, $\Delta p/p = 1\%$). The number of vertical bands (15) determines the maximum momentum acceptance of the COMBAS fragment separator $(\Delta p/p)_{\max} = 15\%$, which is equivalent to particle capture by energy $\Delta E/E = 30\%$. Spacing ΔX between the adjacent vertical bands of the luminophor coordinate grid corresponds to the dispersion of the COMBAS fragment separator, i.e., $\Delta X = 15$ mm per 1% $\Delta p/p$.

The effect of the acceptance value on the collection efficiency of exotic ^{8}He nuclei in final focal plane F_{a1} is demonstrated in Fig. 5.

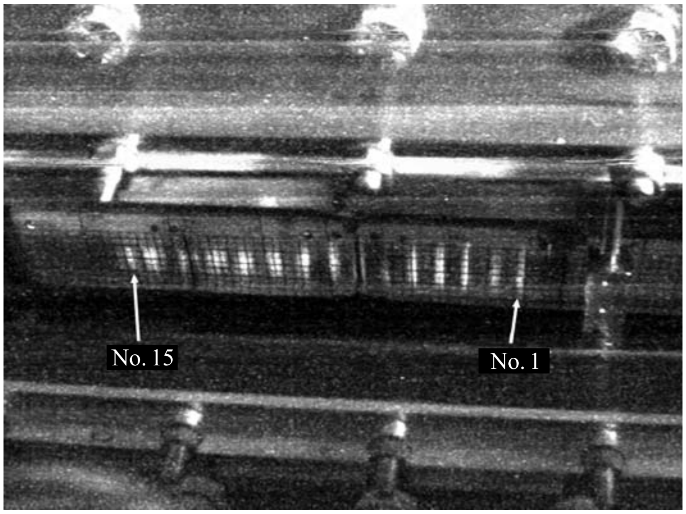

Fig. 4. View of dispersion plane F_d of the COMBAS kinematic separator recorded by a video camera during the experiment with ^{11}B beams with an energy of 33 MeV/A. The set of light vertical bands 1–15 on the coordinate grid of the luminophor platform was obtained by ionizing the luminophor with the primary beam of monochromatic ^{11}B particles upon changing the magnetic rigidity by the first section M_1–M_4 with a step $\Delta B\rho/B\rho = 1\%$ (or, for the momentum, $\Delta p/p = 1\%$)

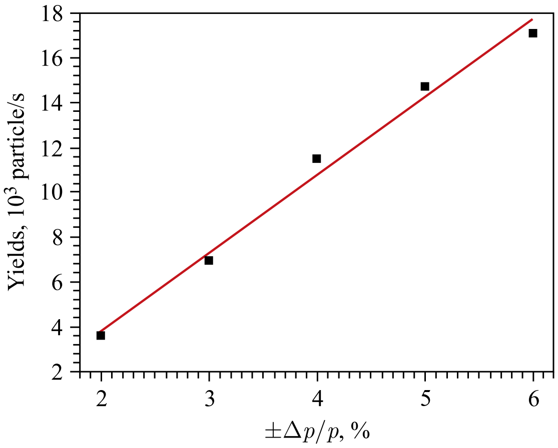

Fig. 5. Variation in the yields of ^{8}He nuclei at final focus F_{a1} with an increase in the momentum acceptance of the COMBAS separator. Measurements of $\pm\Delta p/p$ were taken on both sides, symmetrically with respect to the axial line of the kinematic separator $-\Delta p/p$ and $+\Delta p/p$

In the course of measurements, momentum acceptance $\pm\Delta p/p$ was diaphragmed by the collimator, which slit centroid was matched with the axial line of the kinematic separator, providing the symmetry of quantities $-\Delta p/p$ and $+\Delta p/p$. The ^{8}He beam nuclei were obtained in the fragmentation reaction ^{11}B (33 MeV$/A$) on ^{9}Be target nuclei. The increase in the acceptance from 4% ($\pm\Delta p/p = 2\%$) to 12% ($\pm\Delta p/p = 6\%$) ensured the fivefold increase in the collection of ^{8}He exotic nuclei. This separator property is extremely important in collection of exotic nuclei with a low yield (along the nuclear drip-line). In addition, the significant separator acceptance opens up prospects for the use of thicker producing targets.

The angular acceptance of the products of exchange and fragmentation nuclear reactions also has a strong effect on the collection efficiency of radioactive nuclei. The evolution of collection of ^{8}He nuclei from the reaction ^{11}B (33 MeV/A) $+ {}^9$Be by the COMBAS separator with an increase in the horizontal acceptance angle is shown in Fig. 6. From this figure it follows that the horizontal acceptance angle (for engineering reasons, the entrance angle could be varied only in the median plane) ensuring the increasing collection of ^{8}He nuclei is within ± 30 mrad (approximately $\pm 2^\circ$). It is also apparent that the increase in the collection angle in the range of $\pm 10-30$ mrad (by a factor of 3) causes the nuclear collection efficiency to increase twofold and even more.

The geometrical size of the focused secondary beam of the radioactive nuclei at the final achromatic focus F$_{a1}$ is one of the most important characteristics of the COMBAS kinematic separator which determines the matching of its emittance with the aperture of detector system with minimized losses of impact particles. Figure 7 represents the experimental distributions of beam images for ^{6}He (Fig. 7, a, b) and ^{8}He nuclei (Fig. 7, c, d) in the X and Y coordinates, re-

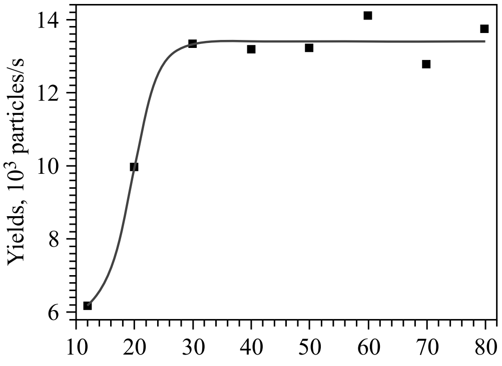

Fig. 6. Evolution of the collection of ^{8}He nuclei versus the angle of horizontal capture by the COMBAS separator

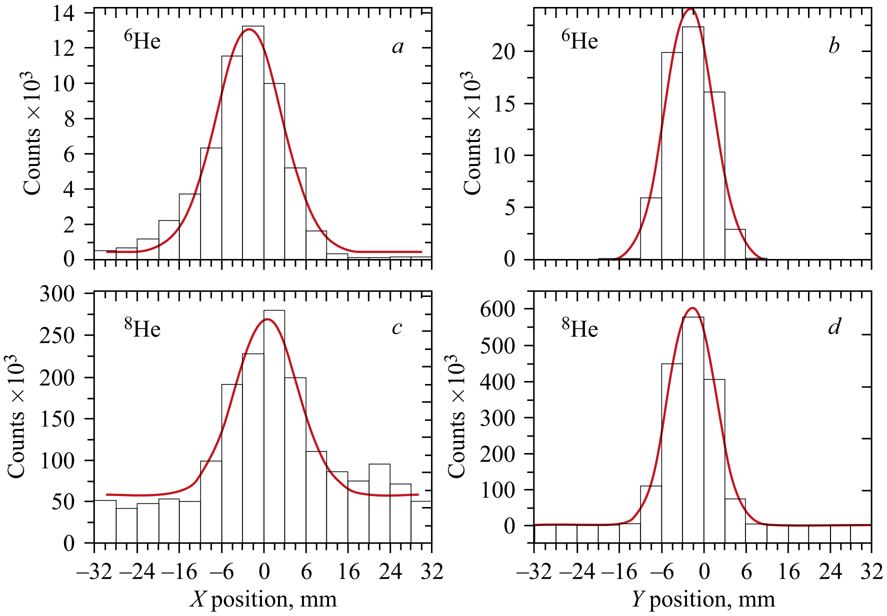

Fig. 7. Distributions of images of ^{6}He (a, b) and ^{8}He (c, d) beams at the final achromatic focus F_a of the COMBAS separator, measured at momentum acceptance $\Delta p/p = \pm 6.6\%$ (or 26.4% for energy) and using the nonprofiled thick (400 μm) Al degrader in dispersion plane F_d: a, c) distributions along horizontal axis X; b, d) distributions along vertical axis Y

spectively. These distributions were measured at a wide momentum acceptance, $\Delta p/p = \pm 6.6\%$. In this case, the primary beam size at the producing target (position F_0) was diaphragmed by the collimator, 6 mm in diameter. In accordance with the figures, the full widths at half maximum of the distributions in the horizontal plane (in the median plane, Fig. 7, a, c) are $X = 12{-}13$ mm for ^{6}He and $X = 16{-}17$ mm for ^{8}He. In the vertical plane, the distribution widths (Fig. 7, b and d) are as follows: $Y = 10$ mm for ^{6}He and $Y = 11$ mm for ^{8}He. The broadening of the ^{6}He and ^{8}He beam sizes along the X axis relative to the Y coordinate at such a high momentum acceptance (the energy acceptance is 26.4%) can be attributed to the energy spread of both ^{6}He and ^{8}He in the thick producing target and in the thick nonprofiled degrader (Al, 400 μm), as well as to the aberration effects in the wide aperture magnets. Therefore, under the actual experimental conditions, the ion optics of the COMBAS separator causes the image of the transported radioactive beam at the position of achromatic focus F_{a1} to increase by factors from 2 to 3.

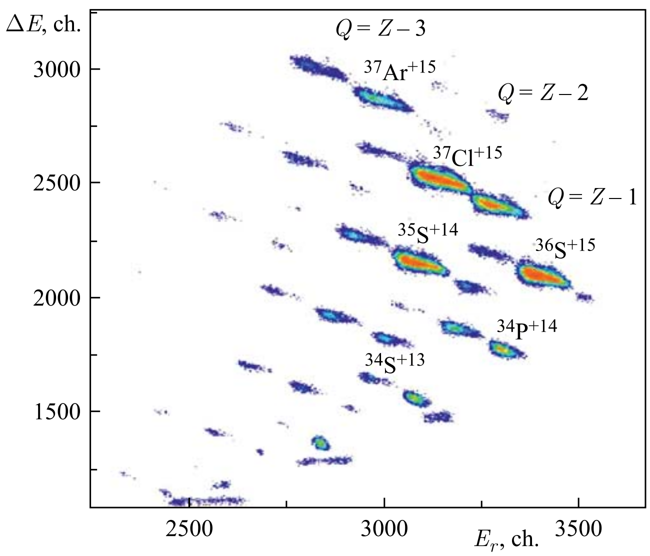

Fig. 8. Identification matrix of products obtained in exchange and fragmentation nuclear reactions ^{40}Ar (40 MeV/A)+^{9}Be. Separated products were detected at final achromatic focus F_a of the COMBAS separator by the $\Delta E \times E_r$ telescope. At the top of the figure, $Q = Z - 3$, $Q = Z - 2$, and $Q = Z - 1$ are the charge states of detected nuclear reaction products

The isotope separating capability of the COMBAS analyzer is illustrated in Fig. 8 [8]. In this figure one can see clear separation of the isotopes — products of the exchange and fragmentation reactions ^{40}Ar (40 MeV$/A$) + ^{9}Be (at a fixed magnetic rigidity) in the test experiment at the COMBAS separator. This indicates that the use of the three-dimensional analysis in the experiment, namely, magnetic rigidity $B\rho$ of the separator, ionization loss $\Delta E/E$ in the penetrating detector, and residual energy E_r, provides a means for reliably identifying nuclear reaction products by A and Z in wide ranges of atomic and mass numbers.

Using the degrader in dispersion plane F_d, it is possible to reduce substantially the intensity of satellite products of ^{40}Ar fragmentation in final focus F_a tuning the rigidity of the COMBAS separating line, in particular, to the ^{39}Cl isotope that is interesting for us. Figure 9 demonstrates the efficiency with which the degrader and the second separator section (M_5–M_8) purify the ^{39}Cl isotope of the massive of satellite nuclear reaction products presented in Fig. 8. The purification efficiency of 70–80% (of the total sum of nuclear reaction products delivered to F_a) has been attained at an optimal selection of the degrader thickness (~ 100 μm Al foil).

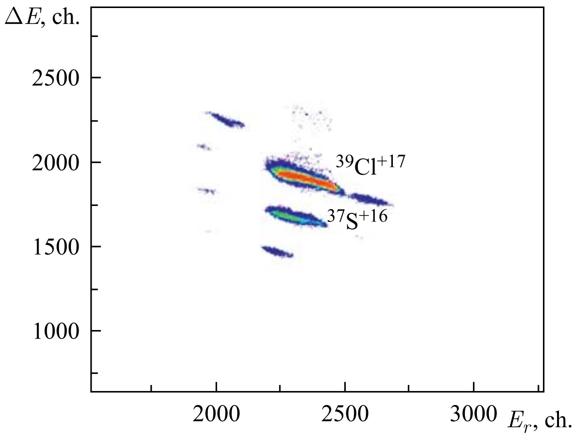

Fig. 9. Identification matrix of nuclear reaction products at achromatic focus F_a upon placing the Al degrader at dispersion focus F_d of the COMBAS separator

Table 1. **Comparison of the parameters of the available kinematic separators. Here Ω is the solid angle; $\Delta p/p$ is the relative momentum acceptance; and $B\rho$ is the magnetic rigidity (invited talk by B. M. Sherrill [9])**

Device	Ω, msr	$\Delta p/p$, %	$B\rho$, T · m	Res. power
LISE [1]	1.0	5.0	3.2	800
A1200 [2]	0.8–4.3	3.0	5.4	700–1500
RIPS [3]	5.0	6.0	5.76	1500
FRS [4]	0.7–2.5	2.0	9–18	240–1500
COMBAS [5]	6.4	20	4.5	4300

The main characteristics of similar kinematic separators, being in operation at research laboratories in France, the United States, Japan, and Germany, are presented in Table 1 for comparison [9].

The advantages of the wide-aperture COMBAS kinematic separator are in momentum $\Delta p/p$ (4–10 times) and angular Ω-acceptances (1.5–6.4 times), as well as in resolution (3–4 times), the values of which are important for increasing the collection of secondary radioactive nuclear beams (Figs. 5 and 6).

1.2. Ion-Optical Channel for Matching the COMBAS Kinematic Separator Emittance with Detector System. The ion-optical channel (Fig. 2) based on quadrupole lenses with diagnostic tracking detectors make it possible:

1) to form more correctly the radioactive nuclear beams being transported to the position of the second target to study the nuclear reactions with secondary beams of radioactive nuclei;

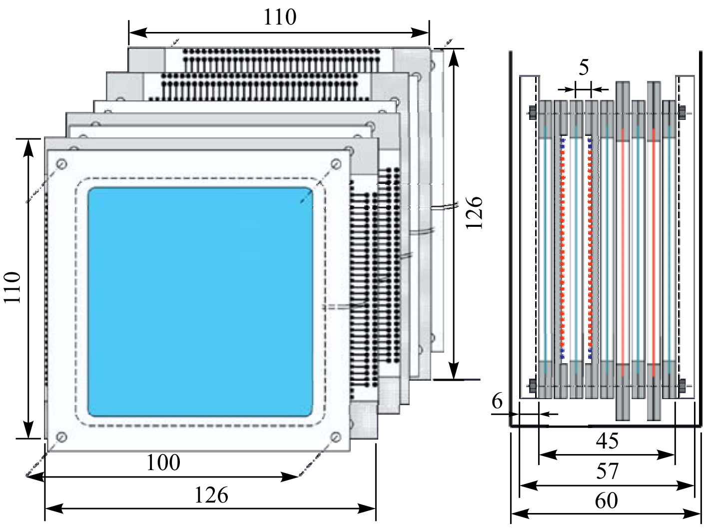

Fig. 10. View of radioactive beam track detector. Cascade from four penetrating proportional chambers (on the two X and Y plates) for determining X and Y coordinates and angular divergences of transported radioactive particles to target position

2) to provide the trajectory analysis of the secondary radioactive beams, to determine the coordinates of the impact projectiles on the target and their angular divergence, and also to monitor the radioactive projectiles intensity;

3) to provide in-flight measurement of the energies for nuclear reaction products, being analyzed in a wide momentum acceptance range of the separator by the time of flight between F_{a1} and F_{a2};

4) to provide the identification of the isotopic composition of the radioactive beams over Z and A by [ΔE, TOF] method using base F_{a1}–F_{a2}.

In Fig. 10, a cascade from two (X, Y) pairs of 32 coordinates penetrating proportional chambers is shown which provide the coordinate resolution in one-mm projectile beams in the target position.

2. THE COMBAS DETECTOR SYSTEM

Research program over the COMBAS kinematic separator uses two alternative detector systems:

1) the telescope from Si and CsI/Tl detectors to identify the whole composition of nuclear reaction products over Z and A [10];

2) the gas-filling multitrack detector (time projection chamber TPC) to reconstruct the complete kinematics of rare multiparticle decays of short-lived unstable nuclei [11].

2.1. The Telescope Detectors. The telescope detector system [10] for kinematic separator COMBAS is constructed from cascade penetrated X- and Y-coordinated detectors of different thickness for measuring the energy losses ΔE (Fig. $11, a$), residue energy E_r (Fig. $11, b$), and the time of flight (TOF) consistent with relationships: $\Delta E \sim (Z/v)^2$, $\Delta E + E_r \sim (Av^2)/2$, and TOF $\sim (1/v)$.

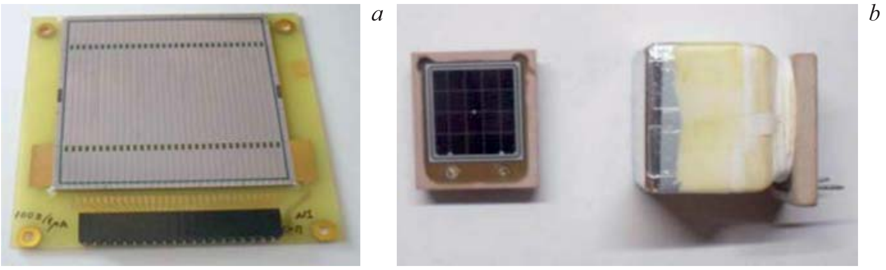

Fig. 11. *a*) View of X- and Y-coordinates 32-strips Si energy losses ΔE detectors with thickness 280 μm (or 380 μm and 1 mm). *b*) View of the residue energy E_r scintillation detectors CsI/Tl 20 mm thick: left — the photosensitive accumulator; right — assembly from the CsI/Tl 20 mm (forward from left) and the photosensitive accumulator (right)

The detector complex is served by the multiparametric registering system. Realized variant of the detector system in combination with magnetic rigidity $B\rho$ provides simultaneous registration of the whole variety of transported particles in the final focus separator COMBAS such as long-ranged particles of light elements Z (to occupy the total thickness of telescope detectors) and short-ranged high-ionized particles with high atomic number Z (to use only several front ΔE detectors of telescope).

In order to detect efficiently the whole variety of nuclear-reaction products produced in the reaction $^{40}\mathrm{Ar}\,(35\ \mathrm{MeV}/A) + {}^{9}\mathrm{Be}\,(15\ \mathrm{mg/cm^2})$ (see, for example, Fig. 8), the (ΔE_1, ΔE_2, and E_r) three-detector telescope was used (Fig. 12).

The ΔE_1 detector is a 32-strip silicon X detector 380 μm in thickness and 64×64 mm in cross-sectional area for measuring the particle coordinate along the horizontal direction. The ΔE_2 detector is a 32-strip silicon Y detector 1000 μm in thickness and 64×64 mm in cross-sectional area for measuring the particle coordinate along the vertical direction. The E detector is a granular assembly of nine full-absorption scintillation detectors CsI/Tl 20 mm thick, the total cross-sectional area of the assembly being 64×64 mm. The strip structure of the ΔE_1 and ΔE_2 detectors played an important role of monitoring the reaction products

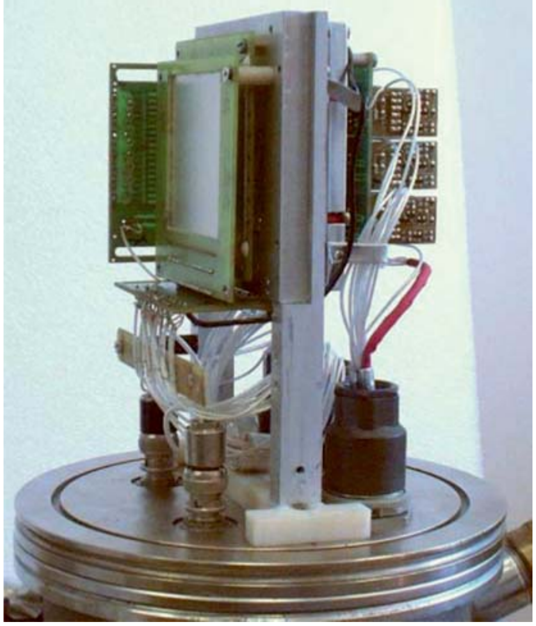

Fig. 12. View of the telescope detector (upper cell)

in the final focus F_a (by tuning to minimal losses in the telescope aperture). In the course of the exposure, the monitoring functions of the strip detectors made it possible also to correct the beam axis in X and Y against the F_a focus.

A ^{9}Be target 15 mg/cm^2 thick was irradiated with a ^{40}Ar primary beam with the energy of 35 MeV per nucleon. The primary-beam spot at the target (position F_0 in Fig. 2) was collimated by means of a diaphragm with an aperture diameter of 6 mm. The intensity of the primary beam incident on the target was measured by a current sensor in μA units. The measurements of the current at the target were then used to normalize the yields of nuclear reaction products to the number of primary beam particles in order to determine also the cross-section production of radioactive nuclei. The momentum distributions of nuclear-reaction products were determined by analyzing the reaction product yields at the final focus F_a versus the magnetic rigidity $B\rho$, which were normalized to the primary-beam current measured in each exposure by the current sensor in μA units. In order to increase the counting rate, the momentum spectra of nuclear-reaction products were scanned with a 2% momentum window whose width was determined by the collimator slit in the dispersion plane F_d.

In order to study the degrader separating ability for isotopes, for example ^{39}Cl, the magnetic rigidity $B\rho$ was set to the value corresponding to the maxima of the momentum distributions for the measured isotopes. The degree of purification of the isotope ^{39}Cl (Fig. 9) produced in the ^{40}Ar (35 MeV/A) + ^{9}Be reaction from satellite reaction products was determined by means of a comparison for the fraction of counts associated with the isotope ^{39}Cl in the total sum of isotopes detected first in the course of a degrader free exposure in F_d. After the insertion of the degrader at F_d, the exposure was repeated in order to determine the fraction of ^{39}Cl counts in the new total sum of detected products. Concurrently, the magnetic rigidity $B\rho$ of the M_5–M_8 (second section) separator must be reduced by the value of the energy loss of the isotope ^{39}Cl throughout the thickness of the Al-foil degrader.

From diagrams in Figs. 8 and 9, one can see that the high dispersion power of the combination of the kinematic separator and the detecting system provides a high resolution and makes it possible to determine the absolute values of A, Z, and Q particles. The admixture of ^{37}S^{+16} ions is about 10%, the total contribution of all other ions, including ^{38,40}Cl and ^{41}Ar, being less than 12%. The total counting rate in the semiconductor telescope used to identify fragments was about 2000 particles per second at the ^{40}Ar primary-beam current of about 100 nA.

2.2. The Gas-Filling Track Detector (TPC). The study of extraordinary decay properties of unstable nuclei near the drip-line with ultra-small yields makes use of the detecting complex which could provide the measurements of a full multiparticle kinematics and simultaneously carry out unambiguous identification of all types of particles with good accuracy. Motivated by such an idea, a luminosity and the high-informative tracking detector (the time projection chamber TPC) was developed that allows three-dimensional reconstruction of multitrack events with a high spatial resolution and identification of charged particles by ionization sampling [11]. Furthermore, the large sensitive gas volume of the TPC and its property to visualize all the tracks of multiparticle process permits one to use effectively the detector TPC itself in the mode detector–gas target–detector. Thus, we can reach the 4π-geometry for simultaneous registration of both the unstable projectile and the nuclei-recoil of the working gas. It is very important since exotic projectiles near the drip-line are produced with very low intensities which therewith will be experienced by the rare multiparticle breakups.

The detector complex with TPC consists of two main devices (Fig. 13):

1) a track detector (in front of the gas-filling TPC, Fig. 10) consisting of a pair of two-coordinate proportional counters which, for each exotic projectile, measures its position, angle and arrival time upstream (trigger) to the gas-filling TPC detector. The proportional counters permit one to register a high intensity of secondary radioactive beams (up to 10^6 pps);

2) TPC detector on the basis of a multilayer drift chambers, identifying over Z projectiles and their decay products (by dE/dx layers) and measuring also the whole track of the decay products induced in the collisions of unstable projectiles with the particles of the gas target.

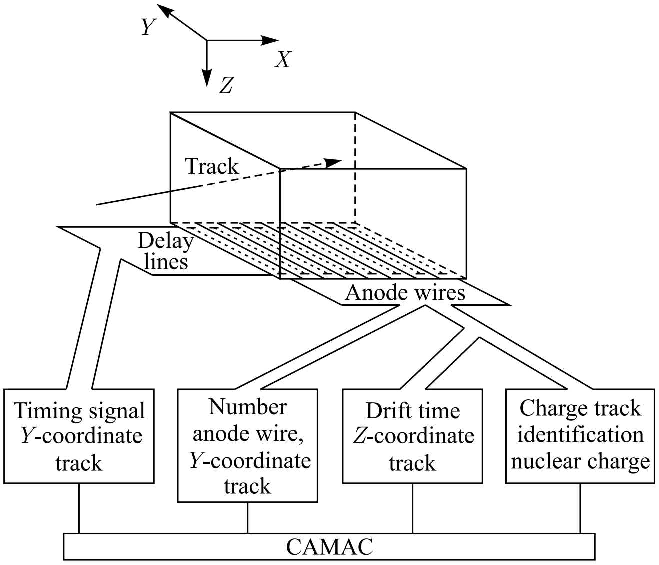

Fig. 13. Schematic principle of the TPC operation

The TPC detector [11] consists of 64 drift layers each 20 mm thick for ionization sampling. Uniform electric field for each drift layer is formed by anode wire of proportional counter. The electron drift-time is used for the measurement of the Z coordinate (vertical). The location of the avalanche along the wire is measured by a delay line (DL). The signal is induced directly in the delay line, and then spreads to both ends. The coordinate in Y-direction (horizontal) is determined by the measurement of the time difference between the arrival of the signals at the left and at the right ends of the delay line. Thus, the one drift layer of TPC chamber provides a two-dimensional position measurement. Furthermore, the amplitude of the anode signal is used to measure the energy loss of ions. Number of electronic channels is: two per each drift layer for Z-, Y-position measurements and the whole of 64 positions for energy loss determination. Gas filling: $\mathrm{Ar} + 10\%\ \mathrm{CH}_4$ at 1 bar pressure. 64 anode wires 20 μm in diameter are placed in the lower part of the TPC (bottom of drift space). Thus dE/dx layers of 20 mm thickness (for example, for our TPC) are formed for the ionization sampling from the drift volume. The number of drift layers can be arbitrary. However, we use only 64 drift layers for the kinematically complete measurements of correlated breakup products and their Z-identification. A block-scheme of the electronics is shown in Fig. 14.

Standard NIM and CAMAC electronics were used. Each of the 64 anode channels is connected to a preamplifier (Pa) and a shaping amplifier (A) with two

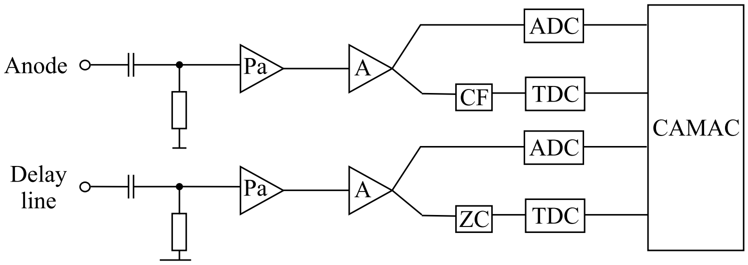

Fig. 14. Basic block-diagram of the analog and timing channels of the TPC electronics

outputs, where the signal is divided in a branch for the energy signal and for the time signal.

The energy signal is sent to a 12-bit ADC. In the time-signal branch, a constant fraction discriminator (CF) provides a logic pulse for the stop signal of the 12-bit TDC with an acquisition time of 5 μs. A common start TPC is supplied by a trigger unit (ahead of the track detector). The signals from the left and right sides of the delay line are treated in the same way, except for the use of zero crossers (ZC) for the logic timing pulse.

As was already shown in experiments with heavy-ion beams [12], the track efficiency of the TPC can exceed 90% for the beam intensity of about $5 \cdot 10^3$ cm$^{-2} \cdot$ s^{-1}. A spatial resolution of $\sigma_z \sim 50$ μm (r.m.s) was accomplished by electron drift-time measurement, the Y coordinate was measured by a cathode delay line with a resolution of $\sigma_y \sim 110$ μm. At the present time TPC complex is in active phase of development.

As 4π-geometry detector, the TPC is a promising detector for studying the correlations of multiparticle decays with simultaneous identification of their Z atomic numbers. This detector is the prospect to study the binary processes of the elastic and inelastic scattering of unstable projectiles (especially drip-line nuclei with ultra-small intensities) on the simplest nucleus (proton) of a gas-filled detector in inverse kinematics (mass of the projectile is larger than the mass of the target particles).

The multitracks attribute of TPC detector can be efficiently used for systematic studying the rare decays of proton-rich nuclei near or beyond the drip-line, for example, for the investigation of direct or beta-delayed proton decay (cluster radioactivity). It is well known that as the ground-state proton drip-line is approached, β-delayed particle emission takes place. In the last process, the particle emission is occurred from the excited states of the daughter nuclei populated in the decay. Experimental investigations of proton radioactivity show that the branch ratio β_{2p}/β_{1p} strongly increases approaching the proton drip-line and that energy decays $Q_{2p} > Q_{1p}$ can occur. In the case of $Q_{2p} > Q_{1p}$ and $Q_{2p} > V_{2p}$

(here V_{2p} is the Coulomb barrier of $2p$-emission), the direct $2p$ emission from unbound nuclei along and beyond the proton drip-line is expected. The existence of the Coulomb barrier V_{2p} in weakly unbound nuclei ($Q_{2p} \leqslant -1$ MeV) with $Q_{2p} < V_{2p}$ leads to the considerable delay of their Coulomb subbarrier decays (τ-delay $\approx 0.1{-}1.0$ ms).

Investigations of the direct $2p$-emission from the ground state exotic nuclei are also possible by the TPC detector. It is predicted that candidates for direct $2p$-emission could be $2p$-unbound nuclei of ^{34}Ti, ^{42}Cr, ^{45}Fe and ^{48}Ni.

3. SCIENTIFIC CONTENT

Production of secondary beams of radioactive nuclei and investigation of the properties of unstable nuclei are the problems of paramount importance in the research programs of the leading centers in the United States, Europe, and Japan, and they are widely discussed at international forums. These investigations are livened up by up-to-date achievements in the acceleration and separation technologies, which provide the means for obtaining secondary beams of short-lived nuclei with a sufficient intensity. Experiments with radioactive nuclear beams have demonstrated that, in nuclei highly asymmetric in N/Z, the structure dramatically evolves from shell-like in the region of stable nuclei to the cluster structure for nuclei near the nucleon drip-line (development of deformations, disappearance of shells with the magic numbers, halo structure, etc.). Therefore, systematic investigations of properties of nuclei with an anomalous N/Z ratio versus the isospin (isospin is proportional to N–Z) will make it possible to study not only the applicability limits of the mean field concept on which various shells model modification is constructed, but also to obtain important information on the properties of nuclear matter with a density differing from the density in stable nuclei. Considerable prospects are also opened up for synthesis of new neutron-rich isotopes of heavy and superheavy elements on secondary radioactive nuclear beams.

3.1. Studying Mechanisms of Nuclide Production at Intermediate Energies and Producing Secondary Radioactive Nuclear Beams. Nuclear reactions with heavy ions at intermediate energies, particularly in the transition region of the Fermi energy, are a matter of profound interest both for studying nuclear dynamics and for obtaining secondary beams of radioactive nuclei with an anomalous N/Z ratio. Nuclear interactions at energies below the Fermi energy are known to be characterized mainly by single-body dynamics and are interpreted in terms of the mean field, since nucleon–nucleon collisions are hindered by the Pauli principle [13]. In the region of the Fermi energy [14–17], the relative velocities of the colliding nuclei become comparable to the inter-nuclear movement of nucleons. A favorable situation is produced thereby for exchange of nucleons between the interacting partners with the outlook for production of nuclei with anomalous N/Z ratio, including the ones near the nucleon drip-line. As the energy of the colliding partners increases, the competitive mechanism of nucleon–nucleon collisions becomes involved into the dynamics of interaction, since the Pauli exclusion principle is removed. At energies above the Fermi energy, the mean field effects become weaker, and the dynamics of nucleon–nucleon collisions becomes predominant. At substantially higher collision energies, the processes of fragmentation and multifragmentation of interacting partners come into force.

Heavy-ion reactions in the transitional Fermi energy domain are complex processes, being a mixture of low-energy dissipative binary processes and fragmentation or multifragmentation processes. In order to understand the heavy-ion reaction mechanism in the Fermi energy domain, it is necessary to answer the questions: (i) how rapidly does reaction mechanism evolve from low to high energy regime? (ii) how does the neutron excess of the projectile and target affect the production of exotic nuclei? (iii) which new phenomena can be met?

The systematic investigations [18–20] of forward-angle characteristics of isotopes with atomic numbers $2 < Z < 11$ produced in nucleus–nucleus collisions of the ^{18}O (35 MeV/A) projectile on the ^{9}Be and ^{181}Ta targets and ^{22}Ne (40 MeV/A) projectile on the ^{9}Be target were carried out using the COMBAS kinematic separator. Two targets with different neutron-to-proton ratio were used to study the influence of the target neutron excess on the neutron-rich isotope production. The inclusive velocity, isotopic and element distributions of projectile-like fragments were measured. The measured velocity distributions of all fragments have asymmetric form with the sharp maximum peaked close to the beam velocity position. The fast velocity component near beam velocity can be attributed to quasi-elastic and to direct breakup transfer reactions. Moving from the projectile mass to light-elements mass region, the contribution of inelastic part systematically increases, the distributions are wider and more asymmetrical. To estimate the contributions of different reaction mechanisms, measured velocity distributions were empirically decomposed into two components: one component centered at beam velocity (called direct) and a dissipative or deep-inelastic component, that peaks at velocities below beam velocity. Using the present known theoretical approaches, the direct component was optimal interpreted in the framework of the Goldhaber model [21] and the dissipative component was analyzed using the two models, namely, Quantum Molecular Dynamics (QMD) [22–24] and Boltzmann–Nordheim–Vlasov (BNV) [15, 17]. Model analysis showed [25–28] that the direct component follows the systematics of the Goldhaber formalism with a width parameter that is in a reasonable agreement, while the transport description (BNV) of the direct component is not reproduced by the calculations and describes mainly the dissipative component of the experimental spectra. A possible reason is, that BNV includes mean field dynamics, and direct nucleon–nucleon (NN) interactions enter only through a collision term. The BNV calculations produce primary fragments with considerable excitation energy. To compare with the experiment, we calculated excitation energy in self-consistent SMM program of Botvina, Mishustin [29]. As a result, the reasonable agreement in isotope distributions is achieved, while the calculated velocity distributions are still narrower and shifted to the lower velocity as compared to the experimental data. We have further investigated the difference in the behavior of two collision systems with a light (beryllium nucleus with small isospin) and a heavy target (tantalum with high isospin), respectively. We see that the mechanism of the two reactions is considerably different. For the lighter target, a greater transparency and smaller dissipation for a given impact parameter is seen, on the other hand, one has contributions from a larger range of impact parameters. For further progress in exploring the nucleus–nucleus reaction mechanisms around the Fermi energy domain and an influence of a mass asymmetry of the colliding system, more refined experiments are needed.

Studying of the yields of neutron-rich and proton-rich isotopes with $3 \leqslant Z \leqslant 40$ in exchange and fragmentation reactions is a matter of interest [30–33] in interactions of heavy projectile nuclei, such as ^{40}Ar, $^{40-48}$Ca, $^{58-64}$Ni, $^{64-70}$Zn, $^{78-86}$Kr, etc., with energies in the vicinity of Fermi energy $E = 20{-}100$ MeV/A, with a light ^{9}Be target (a small isospin parameter), and a heavy target, e.g., ^{197}Au (with the high isospin). In forward-angle measurements, where yields of reaction products at intermediate energies are concentrated, the velocity, isotope, and elemental distributions of radioactive nuclei will be investigated at the COMBAS separator. From these nuclei, it will be possible to form secondary beams of exotic nuclei showing prospects both for synthesis of neutron-rich isotopes of heavy and superheavy elements, and for investigations of nuclear reactions on exotic nuclear beams.

As an example, the production cross sections are presented in Fig. 15 in the form of three-dimensional diagrams for a great number of isotopes, which were predicted for reactions ^{40}Ca (100 MeV/A) + ^{9}Be and ^{48}Ca (100 MeV/A) + ^{9}Be in [33]. From these diagrams, one can see the considerable superiority of the beam based on neutron-rich stable nucleus ^{48}Ca over ^{40}Ca in a wide range of the production cross sections (10^{-6}–10^{2} mb). Fragmentation of ^{48}Ca results in production of a factor of eight greater numbers of neutron-rich isotopes than in a similar reaction with a lighter stable isotope ^{40}Ca.

Using measured (and, for some isotopes, calculated [31–33]) production cross sections for fragments, we can estimate the intensity of promising neutron-rich nuclei expected in fragmentation reactions for ^{48}Ca nuclei with energies of 30–50 MeV/A. Figure 16 represents the evaluated yields of the isotopes for elements from oxygen ($Z = 8$) to scandium ($Z = 22$), which were calculated under the following assumptions: intensity of the ^{48}Ca ion beam, 1 μA; thickness of the producing of ^{9}Be target, ~ 300 μm; and momentum acceptance of the fragment separator, $\pm 2\%$.

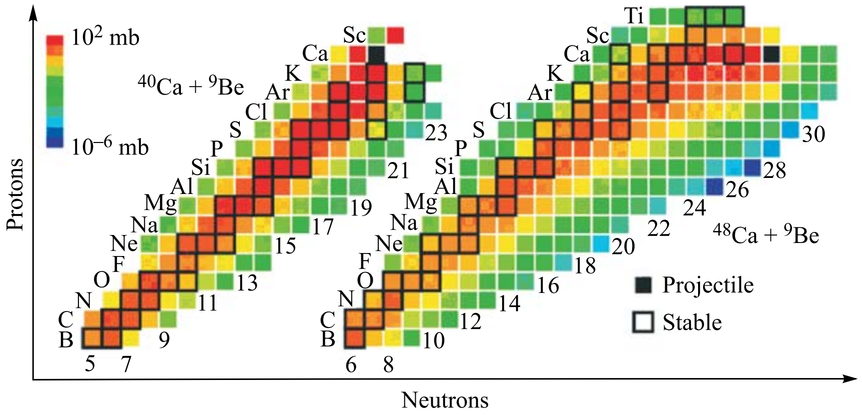

Fig. 15. Three-dimensional diagrams of the cross sections for isotope production in planes N and Z, which were predicted for the fragmentation reactions of ^{40}Ca and ^{48}Ca ions at the ^{9}Be target

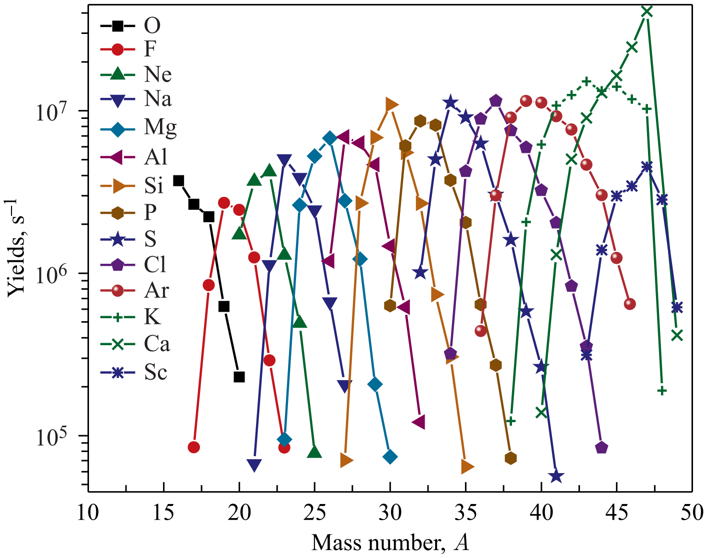

Fig. 16. Expected intensities of neutron-rich nuclear beams predicted for the fragmentation reactions of ^{48}Ca ions with energies in the range of 30–50 MeV/A

From the presented isotope distributions, it is apparent that the intensity of the secondary beams of radioactive nuclei $^{42-47}$K and $^{41-42}$Ar, which are promising for the use as bombarding particles, may be as high as 10^7 s^{-1}. The beam intensity of exotic isotopes of lighter elements may be as high as 10^5 s^{-1}.

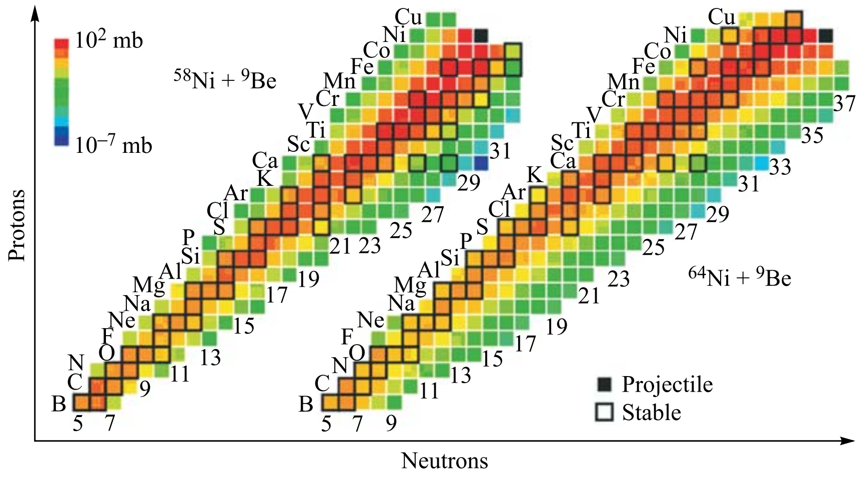

Fig. 17. Three-dimensional diagrams of the cross sections for isotope production in planes N and Z, which were predicted for the fragmentation reactions of ^{58}Ni and ^{64}Ni at the ^{9}Be target

Two isotope patterns expected in exchange and fragmentation reactions for heavier systems of ^{58,64}Ni (30–50 MeV/A) + ^{9}Be are presented in Fig. 17 for comparison. We can also note that the dominating quantity of neutron-rich isotopes is expected on the beams of the heavier bombarding particle ^{64}Ni in comparison with the fragmentation of a lighter nucleus ^{58}Ni. However, this advantage is not so significant as was in the case of ^{48}Ca beams as compared to ^{40}Ca.

3.2. Study of the Nuclear Sizes of Radioactive Nuclei. *3.2.1. Measurement of Total Nuclear Reaction Cross Sections of Unstable Nuclei.* The total nuclear reaction cross sections (σ_R) measurements have for a long time been of interest since they tell us about the radii and transparency of these nuclei and give clues to the understanding of their structure. The nuclear size and density distribution are important bulk properties of nuclei that determine the nuclear potential, single-particle orbitals, and wave function. It is worth to notice that information on nuclear sizes of unstable nuclei, especially exotic isotopes close to the neutron drip line, produced with ultra-small yields in heavy-ions stable beam-induced reactions is extremely difficult to obtain. In most cases the value of σ_R was obtained from analyses of elastic scattering data which are essentially model-dependent. For studies of unstable nuclei, in particular the physical properties of halo nuclei and the neutron skin thickness, it is valuable to know not only the root-mean-square radii (rms), but it is important to know the details of nucleus–nucleus potentials. Our goal is to study the total reaction cross sections by a direct measurement technique (the so-called beam attenuation or transmission method) which allows one to extract model-independent information [34–37].

In this technique, one simply counts the number of beam particles incident on the target $N_{\rm inc}$, and the corresponding number of outgoing particles which have not undergone a reaction in the target $N_{\rm el}$. The difference between these two numbers, $N_{\rm inc}$ and $N_{\rm el}$, represents the number of reactions $N_{\rm reac}$ which occurred in the target for $N_{\rm inc}$ incident particles:

$$\sigma_R = \frac{N_{\rm inc} - N_{\rm el}}{N_{\rm inc}} \frac{A}{\Delta t \cdot N_A}, \tag{3}$$

where Δt is the target thickness; N_A is Avogadro's number.

The corresponding statistical uncertainties associated with the measured value are thus calculated using the difference between these two numbers $(N_{\rm inc} - N_{\rm el})^{1/2}$.

Target-in and target-out measurements are regularly performed. This procedure is important to exclude the projectile counts from beam collimators and to trigger penetrating ΔE counter. Thus, by subtracting the number of reaction events (normalized to the incident beam intensity) with and without the target, one could obtain the real contribution from the desired total reaction cross section.

Measurement by this luminosity technique is an effective method for determining σ_R of unstable nuclei with high precision in spite of low projectile intensities. The total nuclear reaction cross sections (σ_R) can be measured within a few percent accuracy even with very low intensities of secondary beams of radioactive nuclei near drip-lines.

To determine the nuclear radius from measurements of the total reaction cross section (σ_R) at low-energy nuclear reactions, the following analytic expression is used:

$$\sigma_R = \pi \lambda\!\!\!^{-2} \sum_{l}^{\infty} (2l+1) T(l), \tag{4}$$

where $\lambda\!\!\!^{-}$ is the projectile reduced wavelength; l is the angular momentum; $T(l)$ is the transmission coefficient.

In this model one is supposed that a reaction occurs whenever substantial contact reaches between nuclear matters of projectile and target partners. To describe low-energy nuclear reactions, a strong absorption model was originally developed. In this framework, the sharp cutoff approximation was used, namely $T(l) = 1$ for $l_{\rm crit}$; otherwise, $T(l) = 0$. As a result, one obtains

$$\sigma_R = \pi \lambda\!\!\!^{-2} (l_{\rm crit} + 1)^2 = \pi R_{\rm int}^2 \left(1 - \frac{D}{E_{\rm cm}}\right), \tag{5}$$

where $R_{\rm int}$ is the strong absorption radius; D is the l-dependent potential barrier height. From this relation one can see that σ_R saturates with increasing beam energy at the so-called geometrical value (πR_{int}^2). However, it is known from experiments that the observed decrease of σ_R deviates significantly (above 20–30 MeV/A) from the geometrical limit predicted by this model.

For reproduction of the variation of σ_R over the whole energy range several microscopic approaches have been developed in order to take correctly into account: i) the trajectory deflection of the projectile and ii) the difference between the neutron and proton distributions in N/Z asymmetry exotic nuclei.

Thus, for a nucleon–nucleus collision, the physical ingredients of calculations are simply (i) the matter density distribution of the target, and (ii) N–N total scattering cross sections σ_{nn} averaged over isospin. These quantities are used to construct a local mean free path.

In nucleus–nucleus collisions the mean free path of the projectile is obtained by averaging over the mean free path of the different incident nucleons in the target. This is achieved by constructing the volume overlap of the interacting nuclei. At a given distance (r) between the centers of the colliding nuclei, the local mean free path of the projectile in target can be reproduced. After integrating the local mean free path over the whole trajectory of the projectile, one obtains the probability for N–N interaction $T_0(b)$ at a given impact parameter (b).

Within this microscopic model, σ_R is then derived by assuming that any N–N scattering process leads to a nuclear reaction event between the complex colliding nuclei. Under this assumption, σ_R is related to $T_0(b)$ by the following relation:

$$\sigma_R = \int_0^\infty 2\pi b[1 - T_0(b)]\, db, \tag{6}$$

where (b) is the classical distance of the closest approach of the projectile in the Coulomb plus nuclear potential, $T_0(b)$ is the transmission coefficient.

The trajectory calculations for each impact parameter (b) are fulfilled to include deflection of the projectile. Microscopic models employ total cross sections for free N–N scattering and also took into account the Pauli exclusion principle. Nuclear matter distribution has expressed a simple Gaussian shape. Its shape is deduced semi-empirically to reproduce the tails of the nuclear matter distribution. This is explained by the fact that the σ_R variations are mainly governed by the most peripheral collisions and thus related to the nuclear surface shapes.

However, the modern experimental investigations have shown that in nucleus–nucleus collisions at intermediate bombarding energies, new effects should be included as neutron skin, mass asymmetry, and the Pauli “blocking” especially while using the neutron-rich projectiles. To describe correctly the trends of measured σ_R for unstable projectiles, new phenomenological parameterization for σ_R

was developed by including the transparency and mass asymmetry effects.

$$\sigma_R = \pi R_{\rm int}^2 \left[1 - \frac{B_c}{E_{\rm cm}}\right], \tag{7}$$

where B_c is the Coulomb barrier of the projectile–target system

$$B_c = \frac{Z_t Z_p e^2}{r_c(A_t^{1/3} + A_p^{1/3})}, \tag{8}$$

where $r_c = 1.3$ fm, $Z_{p(t)}$ are the atomic numbers of target and projectile nuclei; $A_{p(t)}$ are their mass numbers; $R_{\rm int}$ is the interaction radius. The latter quantity $R_{\rm int}$ is divided into volume (vol) and surface (surf) terms:

$$R_{\rm int} = R_{\rm vol} + R_{\rm surf}. \tag{9}$$

In order to take into account the effects of σ_R rise at the smaller impact parameters, there was proposed a new parameterazition as a volume (or core) component of the interaction radius $R_{\rm vol} = r_0(A_p^{1/3} + A_t^{1/3})$, where r_0 is a reduced interaction radius. The second component of the interaction radius is a nuclear surface contribution which was parameterized in the following way [34, 35]:

$$R_{\rm surf} = r_0 \left[a \frac{A_p^{1/3} A_t^{1/3}}{A_p^{1/3} + A_t^{1/3}}\right] - c. \tag{10}$$

The first term in the large parentheses is the mass asymmetry term, which is related to the volume overlap of projectile and target, and c is the energy-dependent parameter which takes care of increasing surface transparency as the projectile energy increases. The values of the parameters r_0 and a have been adjusted by using a χ^2 minimizing procedure. To take into account more correctly the neutron skin for the target and projectile, the new parameterization of $R_{\rm surf}$ was proposed:

$$R_{\rm surf} = R_{\rm surf} + D, \tag{11}$$

where the neutron excess term D can be expressed as

$$D = \frac{S(A_t - 2Z_t)Z_p}{A_p A_t}. \tag{12}$$

As a result, the reaction cross section is written as

$$\sigma_R = \pi r_0^2 \left[A_p^{1/3} + A_t^{1/3} + b\frac{A_p^{1/3} A_t^{1/3}}{A_p^{1/3} + A_t^{1/3}} - c(E) + D\right]^2 \left(1 - \frac{B_c}{E_{\rm cm}}\right), \tag{13}$$

where $b = 1.85$ is the asymmetry parameter; $c(E) = 0.31 + 0.014E/A_p$ is the energy-dependent transparency and B_c is the Coulomb barrier.

With a new parameterization the main aspects of the behavior of (σ_R) for nucleus–nucleus collisions at intermediate energies were satisfactory reproduced [34–37].

With the COMBAS kinematic separator, a number of the measurements of the total reaction cross sections (σ_R) for weakly-bound ^{6,8}He, ^{8,9}Li with energies of 15–33 MeV/A using $^{\rm nat}$Al, $^{\rm nat}$Ta, and $^{\rm nat}$Pb targets were carried out [38]. A secondary beams of ^{6,8}He and ^{8,9}Li were produced by bombardment of the ^{11}B (33 MeV/A) primary beam of a Be (89 mg/cm^2) target and separated by the COMBAS kinematic separator. In dispersive focal plane (F_d), a horizontal slit defined the momentum acceptance as 1%, and a wedge degrader of 200 μm Al was installed. The $B\rho$ of a second section of kinematic separator (after F_d) was adjusted for measurements in the energy range 15–33 MeV/A.

The position of secondary radioactive beam at the reaction targets ($^{\rm nat}$Al, $^{\rm nat}$Ta, and $^{\rm nat}$Pb) was determined by parallel-plate avalanche counters and a collimator (∅ 15 mm). Time of flight (TOF) between RF (radio frequency) cyclotron and ΔE (100 μm thickness) detector (before the reaction target) was determined. After the secondary reaction targets, the scattered particles were detected by two Si ΔE detectors 300 μm (32 horizontal striped detector with the size 64×64 mm and 1000 μm (32 vertical striped detector with size 64×64 mm) and by an array of nine (3×3) E_r-detectors from scintillation CsI(Tl) wall. This mosaic consisted of nine CsI(Tl) granules (each granule of 8×18 mm surface and thickness 20 mm) and allowed one to focus the secondary beam. The detector system was allowed to perform both the Z and A identification of the radioactive projectile of the cocktail of the secondary beams and to identify the event of the reaction product scattering on the secondary targets ($^{\rm nat}$Al, $^{\rm nat}$Ta and $^{\rm nat}$Pb). Reaction events are then identified as those whose total energy loss in the telescope differs from that of nonreacting projectiles.

The measurements of total reaction cross sections (σ_R) for weakly-bound ^{6,8}He and ^{8,9}Li on the $^{\rm nat}$Al and $^{\rm nat}$Pb targets at energies 15–33 MeV/A were performed and the results were compared with the previous experiments [35–37]. In the range of 10% accuracy there is an agreement with known data. Strong absorption radii (r_0) were extracted from the measured total reaction cross sections for weakly-bound ^{6,8}He and ^{8,9}Li neutron halo nuclei. The most agreeable estimations of strong absorption radii (r_0) are achieved with the use of new $R_{\rm int}$ parameterization (Eq. (13)).

The success of the transmission method shows that measurements of the cross sections of unstable projectiles near drip-lines with very low intensities with the use of Si telescope are feasible and very informative.

Therefore, in perspective σ measurements for heavier exotic projectiles with $2 < Z < 12$ over energies 20–50 MeV/A (Fermi energy domain) on targets in a wide range of mass (from proton $Z = 1$ up to uranium $Z = 92$) would be actual for testing theoretical models.

3.2.2. Studying of Elastic Scattering of Exotic Nuclei. It is expected that large elastic scattering cross sections will ensure sufficient sensitivity and a high information value in experimental investigations of the properties of exotic nuclei [39–43]. These nuclei are usually obtained in reactions of nucleon exchange or fragmentation with low intensities ($\sim 10^6$ particles/s and less). It is known that the elastic scattering cross section for heavy ions at intermediate energy exhibits Fraunhofer oscillations in the forward angular range which are interpreted as the interference between scattering amplitudes from both sides of the target nucleus, namely, an interference of particle scattering in a positive angle (near-side) and negative angle (far-side). The small forward angular range corresponds to the far peripheral collisions. Therefore, we may conclude that the elastic scattering cross section is determined by the tails of the single-particle distributions of nuclear matter at the periphery of a nucleus. For this reason, one would expect that the experiments on the elastic scattering can give an important information both on the rms radii of single-particle distributions of the nuclear matter and on the details of the nucleus–nucleus potential at very low densities of the nuclear matter at the periphery. It is well known that the angular period of the Fraunhofer oscillations $\Delta\theta$ determines the radius of the strong nuclear absorption by the following simple relationship: $\Delta\theta = \pi/(kR_{\mathrm{abs}})$, where k is the wave number, and R_{abs} is the radius of strong absorption.

Systematic experimental study of the neutron drip-line position in C, N, O isotopes has shown that $N = 16$ neutron number is a new shell closure, while the shell closure at $N = 20$ seems to disappear for Ne and heavier neutron-rich nuclei on the contrary region of stable nuclei. The evidence of “magic losses” at $N = 20$ shell closure and occurrence of a new neutron magic number have been interpreted as “the collapse of the shell model” and force one to revise its basis radically [39].

In the experiments over the elastic scattering, it is planned to study an evolution of the nucleus shape of unstable nuclei with an increase in the neutron excess for isotopes near $N = 20$ shell closure, namely, heavy isotopes of elements Ne, $^{23-32}$Na and Al [42].

The optimal reaction for the production of the proposed heavy isotope group of Ne–Al light elements seems to be ^{40}Ar fragmentation within the energy region 50–100 MeV/A.

The full-scale analysis of the binary processes of elastic and inelastic scattering indicated that the experiments with unstable projectiles can be effectively realized on the TPC detector with the use of the proton target of the gas-filled detector (methane composition CH_4) in the inverse kinematics (mass projectile larger than mass gas–target).

Investigations of elastic scattering cross sections of unstable nuclei on the nucleon (proton) are very interesting because of their sensitivity basically to nucleon–nucleon component of the nuclear reaction ($p-p$ and $p-n$ collisions). In addition, these experimental results are convenient for theoretical analysis because this simplifies the problem of interpretation of the obtained data by excluding the structure of the simplest proton recoil-nuclei.

In the inverse kinematics by the use of TPC one can measure:

1) the tracks of both partners simultaneously;

2) the scattering angles of both nuclei (angular correlations);

3) the energies of both partners (on the ranges and stopping-power);

4) the trajectory entry of projectile previous to scattering position gas–target;

5) the excitation function (measurement of nuclear reaction cross sections versus projectile energy by slowing them in the course of stopping processes);

6) separation of inelastic and elastic processes with sufficient accuracy.

The calculated elastic angular distributions of ^{23,32}Na particles in the laboratory system and the elastic angular distributions of associated recoil-proton partners induced in reactions ^{23,32}Na (35 MeV/A) $+\,p$ in inverse kinematics are shown in Figs. 18 and 19, respectively. As is seen from Fig. 18, the projectile angular distribution is focused in the narrow forward cone ($\theta_{\rm lab}^{\rm Na} < 2°$). In this situation, the registration of elastic projectile demands to provide the very high angular resolution, while the correlated recoil-protons (Fig. 19) have a wide angular distribution (up to $\theta_{\rm lab} = 90°$), which is very convenient for the registration.

Taking into account the very low expected intensities of the ^{32}Na exotic beam and sharp exponential slope of their differential elastic cross sections (see Figs. 18, 19), it is reasonable to assume that only the second and third minima of angular distributions can be reached in the experiments. For the ^{32}Na projectile, this corresponds to the angular region $\theta_{\rm lab}^{\rm Na} = 0-2°$, while for correlated recoil-protons the angular region is $\theta_{\rm lab}^{p} = 50-90°$, respectively. Appropriate angular region for proton detection permits one to use effectively a coincidence

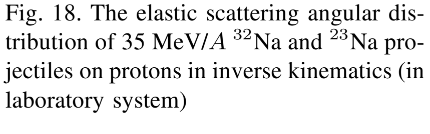

Fig. 18. The elastic scattering angular distribution of 35 MeV/A ^{32}Na and ^{23}Na projectiles on protons in inverse kinematics (in laboratory system)

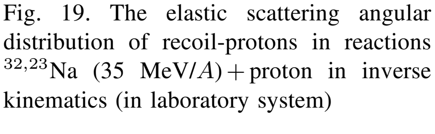

Fig. 19. The elastic scattering angular distribution of recoil-protons in reactions ^{32,23}Na (35 MeV/A) $+$ proton in inverse kinematics (in laboratory system)

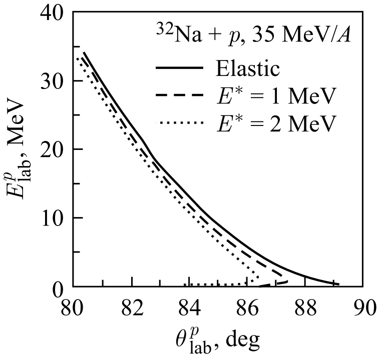

Fig. 20. The energy distribution versus scattering angles of recoil-protons $[E^p_{\rm lab}, \theta^p_{\rm lab}]$ at three energies of the ^{32}Na projectile in the lab. system

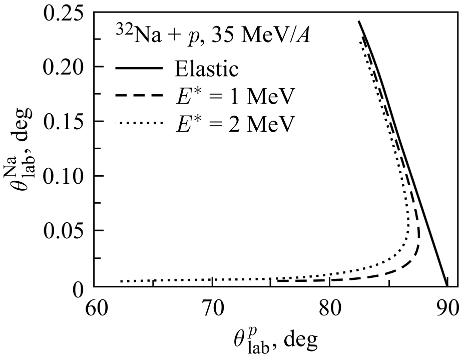

Fig. 21. The function of angle–angle correlations $[\theta^{\rm Na}_{\rm lab}, \theta^p_{\rm lab}]$ of projectiles and recoil-protons at three energies of the ^{32}Na projectile in the lab. system

technique for the registration of correlated projectile and recoil-proton in order to separate the contributions of inelastic scattering into elastic scattering using only Z-identification of recoil-protons. On this reason, the maximum angular sensitivity of TPC must provide an angular region of maximum concentration of recoil-protons $\theta^p_{\rm lab} = 50{-}90°$, which contains the 2nd and 3rd maxima of angular distribution.

In Fig. 20, the energy distributions versus scattering angle of recoil-protons $[E^p_{\rm lab}, \theta^p_{\rm lab}]$ for three energies of the ^{32}Na projectile are shown, and in Fig. 21, $[\theta^{\rm Na}_{\rm lab}, \theta^p_{\rm lab}]$ angle–angle correlations of projectiles and recoil-protons are shown. From Figs. 20 and 21, one observes the high-energy and angular separation of recoil-proton distributions under very small variations of projectile energies. This factor can be effectively used to separate elastic and inelastic scattering processes in case of realization of sufficient angular accuracy and energy in recoil-proton measurements.

Thus, in order to separate inelastic processes from elastic with the accuracy $\Delta E = E^*(\text{energy excitation}) = 1$ MeV, it is necessary to realize angular resolution better than 0.5° for recoil-protons and better than 0.1° for the projectile. The spatial resolution of the TPC chamber is sufficient to reach the necessary angular resolution better than 0.5°.

Just now one makes the estimations of the necessary integral beam and exposure time for the elastic scattering measurements of radioactive nucleus of ^{32}Na with 35 MeV/A energy. In Table 2, the calculated cross sections $\sigma_{\rm reac}$ and elastic cross sections for reactions $^{23,32}{\rm Na} + p$ in the angular bins corresponding to the 2nd and 3rd maxima and their sums are presented.

Assuming 4π-detecting efficiency of TPC, the number of ^{32}Na 35 MeV/A elastic interactions by protons (CH$_4$ gas-filled TPC) under one atmosphere pres-

Table 2. **The calculated cross sections $\sigma_{\rm reac}$ and elastic cross sections for reactions ^{23,32}Na $+\,p$ with 15, 35, 50 MeV/A energies in the angular bins corresponding to the 2nd and 3rd maxima and their sums, respectively**

Nuclide	E, MeV/A			σ, mb
	15	35	50	
^{23}Na	883	711	472	$\sigma_{\rm reac}$
	1050	980	730	$\Delta\sigma_{\rm el}$ (2nd)
	1170	1080	790	$\Delta\sigma_{\rm el}$ (2nd + 3d)
^{32}Na	1326	1185	688	$\sigma_{\rm reac}$
	1100	1100	976	$\Delta\sigma_{\rm el}$ (2nd)
	1180	1140	1120	$\Delta\sigma_{\rm el}$ (2nd + 3d)

sure is equal to $n_p\Delta\sigma$ (2nd) $\approx 1.1\cdot 10^{-4}$ cm^{-1}, where the proton concentration $n_p \approx 10^{20}$ cm^{-3} and $\Delta\sigma$ (2nd) $\approx 1.1\cdot 10^{-24}$ cm^2 (see Table 2). The n_p calculations take into account the protons in the CH$_4$ molecule $n_p \approx N_A\cdot 4/22400 \approx 10^{20}$ cm^{-3}, $N_A = 6.2\cdot 10^{23}$ being Avogadro's number. The sensitive length L of TPC is 50 cm, therefore $n_p\Delta\sigma$ (2nd) $\cdot\, L \approx 5\cdot 10^{-3}$. To achieve 1% accuracy of measurement about 10^4 events are required. In this case we should use $10^4/1.1\cdot 10^{-4} \approx 10^8$ particles of ^{32}Na projectiles. If we have the ^{32}Na intensity equal about 10^2 s^{-1}, then the exposure time of the experiment is $\Delta t \approx 10^8/10^2 = 10^6$ s ≈ 10 days. This exposition is sufficient for measurements in the region of the first and second diffraction maxima.

There is an opportunity to increase the efficiency of the experiment. The number of working protons can be increased considerably by using a series of mylar insulating foils (targets) with thickness $\sim 50\mu$ on the beam trace in the sensitive TPC volume. These additional mylar targets should be installed inclined into two axes in order to exclude the losses of low-energy recoil protons in the 60–90° angular region. The additional targets allow one to increase the total density of protons to a factor of ten and, therefore, to decrease respectively the exposure time. This procedure can, in principle, help one to achieve the higher diffraction maxima region.

3.3. Studying the Cluster Structure of Light Element Nuclei near the Nuclear Drip-Line. To understand the mechanism of structural changes in nuclei with increasing isospin, we are planning to study evolution of the cluster structure with the increase of the neutron excess N/Z in the chain of light-element isotopes $^{6-11}$Li, $^{9-14}$Be, and $^{10-17}$B.

In the theoretical studies [44–47], a substantial intensification of clustering in neutron-rich nuclei of light elements is predicted (an example for the boron isotope is shown in Fig. 22).

This results in a significant increase of the deformation of nuclei while approaching the nuclear drip-line. In deformed nuclei, the ratio of the surface to

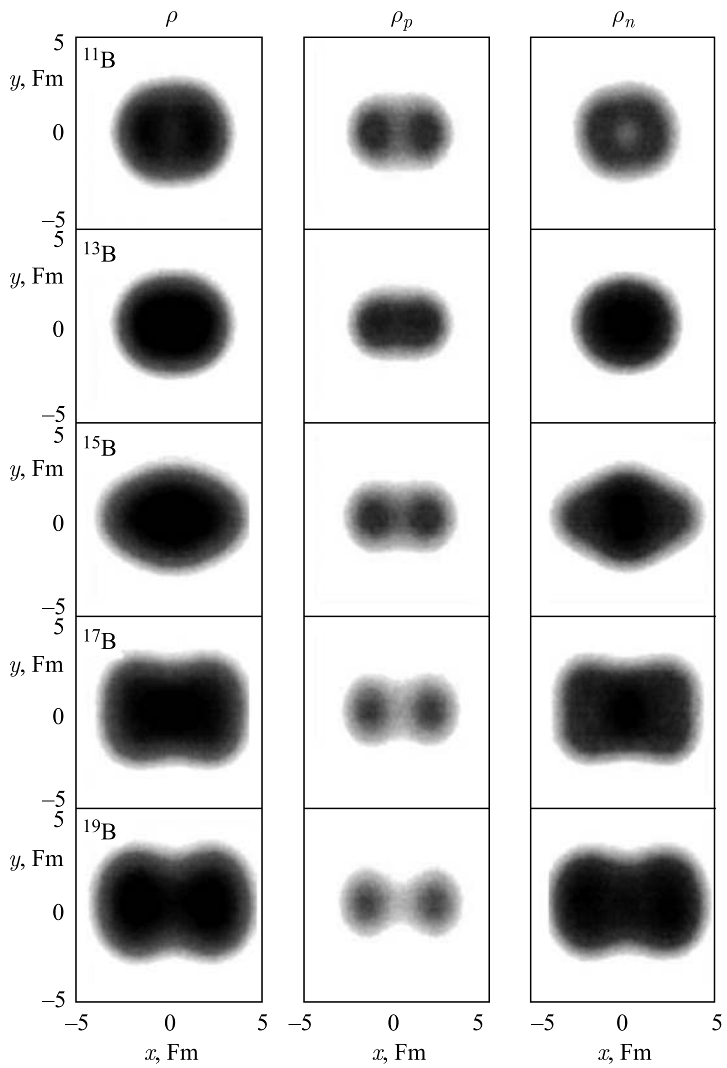

Fig. 22. Simulated projections of neutron (ρ_n), proton (ρ_p), and nucleon (ρ) density distributions. Axes X and Y are graduated in fermi units (Fm)

the volume increases, which stimulates increase of the neutron skin volume in clusterized nuclei. The threshold energies of breakup into clusters and the neutron emission energies are presented in Fig. 23 for Li, Be, and B isotopes. According to the figure, the neutron separation energy in the presented chains of the Li, Be, and B isotopes decreases with an increase in the neutron excess, whereas

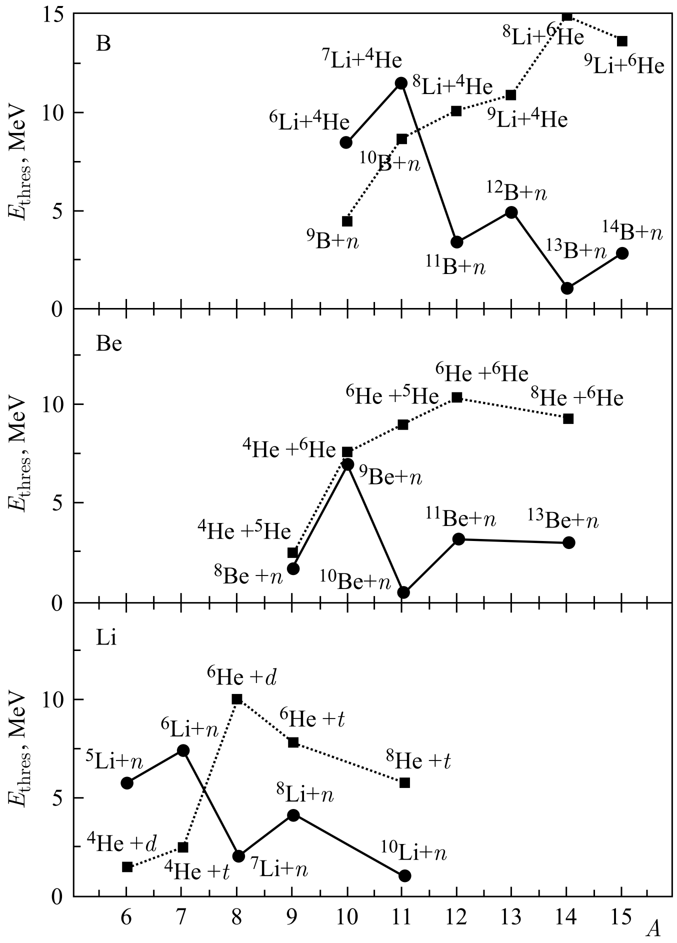

Fig. 23. Threshold energies $E_{\rm thres}$ of breakup into clusters and neutron emission for a group of isotopes Li, Be, and B

the breakup threshold energy of cluster decay increases. Therefore, a search for cluster resonances in nuclei should be performed at high excitation energies (up to several tens of MeV) in the region where the continuum of single-particle excitation dominates.

For obtaining the spectral information over cluster resonances according to unstable nuclei, one proposes a method of “active correlations” [48, 49] for determining the relative energy of breakup products. This method can provide radical suppress of background by registrations of correlations in the real time scale.

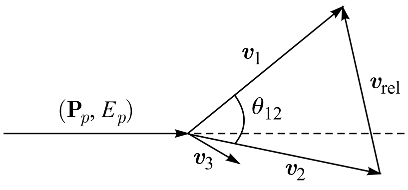

Fig. 24. Velocity diagram for the two-particle Coulomb breakup of ^{11}B nucleus with momentum $\mathbf{P}_p$ and energy E_p into ^{4}He and ^{7}Li clusters, which was initiated in reaction ^{11}B (35 MeV/A) + ^{12}C: ($\boldsymbol{v}_1$, $\boldsymbol{v}_2$, $\boldsymbol{v}_3$, and $\boldsymbol{v}_{\rm rel}$) velocities of ^{4}He, ^{7}Li, and recoil nucleus ^{12}C and relative velocity of the clusters, respectively; and θ_{12} is the opening angle of clusters

Using the momentum and energy conservation laws for the Coulomb breakup, we obtain the known expression for the relative energy: $E_{\rm rel} = (1/2)\mu V_{\rm rel}^2$, where $E_{\rm rel}$ is the relative energy of the fragments produced from Coulomb breakup of the parent nucleus, and μ and $\upsilon_{\rm rel}$ are the reduced mass and relative velocity of the breakup fragments. The velocity diagram for the two-particle breakup of ^{11}B nucleus into clusters ^{4}He and ^{7}Li, initiated in the reaction ^{11}B (35 MeV$/A$) + ^{12}C, is shown in Fig. 24. In this case, the relative energy $E_{\rm rel}$ can be expressed by the following relationship:

$$E_{\rm rel} = \frac{A_2 E_1}{A_1 + A_2} + \frac{A_1 E_2}{A_1 + A_2} - 2(A_1 + A_2)\cos\theta_{12}(A_1 E_1 A_2 E_2)^{1/2}, \qquad (14)$$

where A_1 and A_2 are the mass numbers of ^{4}He and ^{7}Li clusters, respectively; E_1 and E_2 are the kinetic energies of the ^{4}He and ^{7}Li clusters, respectively; and θ_{12} is the opening angle of two clusters.

Measuring kinetic energies of both correlated breakup products in coincidence and their opening angle θ_{12}, we obtain the spectral function of cluster excitations of a nucleus $E^* = E_{\rm rel} - Q_{\rm gg}$, where $Q_{\rm gg}$ is the threshold of nuclear breakup into clusters. From Eq. (14), it is apparent that the spectral function of the cluster resonances depends only on the kinematical parameters of the breakup products E_1, E_2, and θ_{12} and does not depend on projectile energy E of decaying particle. This factor makes it possible to use nonmonochromatic (with a high energy spread) secondary beams of nuclei–candidates for cluster breakup. This is particularly important in studying the structure of exotic nuclei along the nucleon drip-line, which are produced with small cross sections and wide momentum distributions. Moreover, it is also possible to use thicker producing targets to obtain the required intensity of exotic nuclei.

The method for coincidence detection of correlated products has the following advantages [49]:

i) the high selectivity for extracting cluster states from a spectrum of high density particle excitations (in the region of high excitations);

ii) the high kinetic energies of decaying exotic nuclei (30–50 MeV$/A$), which allows one to use effectively the kinematical factor of the forward angle focusing in the laboratory system (particularly, in reactions with inverse kinematics);

iii) owing to the high selectivity of the coincidence method, the possibility of extending the angular range of breakup product measurements to the region of very small angles (around 0°), where data are very sensitive to the value of transferred angular momentum in the reaction, which is a matter of principal importance, since clusters in nuclei are formed in high spin states.

The energy and angular correlations of $^{6-11}$Li, $^{9-14}$Be, and $^{10-17}$B breakup products are planned to be measured in the plane and beyond the plane of the reaction. This will provide the means not only for studying the spectral function of resonances, but also for determining the resonance spins without recourse to the model representations.

It is expected that obtained information will be important both for estimating the applicability limits of the shell model in the nuclear theory [39] and for understanding the fundamental aspects of many-body nuclear dynamics [50]. Beams with required intensities [18, 20] of the above-mentioned light element isotopes have been obtained and separated at the COMBAS fragment-separator (Table 3).

As could be seen from Table 3, the fragmentation reactions of stable ^{18}O and ^{22}Ne projectiles at intermediate energies of 30–50 MeV/A are optimal for obtaining beams of ^{9,11}Li, $^{11-14}$Be, and $^{13-17}$B nuclei.

Table 3. **Production rates of neutron-rich isotopes of elements Li, Be, B, C, and N, obtained in reactions ^{18}O (35 MeV/A) + ^{9}Be and ^{22}Ne (40 MeV/A) + ^{9}Be at a target thickness of 200 mg/cm^2 and primary beam intensity of 5 μA**

Isotope ($\tau_{1/2}, s$)	Rates, pps	
	^{18}O (5 $e\mu$A, 35 MeV/A)	^{22}Ne (5 $e\mu$A, 40 MeV/A)
^{9}Li (0.18)	$2.5 \cdot 10^5$	
^{11}Li (0.008)	$3 \cdot 10^3$	
^{11}Be (13.8)	$1.5 \cdot 10^5$	
^{12}Be (0.024)	$1.5 \cdot 10^5$	
^{14}Be (0.004)	$3 \cdot 10^2$	
^{13}B (0.017)	$1 \cdot 10^6$	$1 \cdot 10^6$
^{14}B (0.014)	$2.5 \cdot 10^5$	$5 \cdot 10^5$
^{15}B (0.01)	$1.5 \cdot 10^5$	$5 \cdot 10^4$
^{17}B (0.005)		$4 \cdot 10^2$
^{15}C (2.45)	$5 \cdot 10^6$	$2 \cdot 10^6$
^{16}C (0.747)	$1 \cdot 10^7$	$5 \cdot 10^5$
^{17}C (0.19)		$1 \cdot 10^5$
^{18}C (0.09)		$1.5 \cdot 10^5$
^{17}N (4.17)		$5 \cdot 10^5$
^{18}N (0.63)		$1 \cdot 10^6$
^{19}N (0.33)		$1.5 \cdot 10^6$

In the future, the program of cluster structure investigations will be extended by including promising nuclei of heavy carbon, nitrogen, and oxygen isotopes. Studies of the cluster structure evolution with increasing neutron excess in a chain of oxygen isotopes $^{16-24}$O are a matter of particular interest, since they can shed light on the experimentally observed instability of oxygen ^{26}O and ^{28}O especially with magic number $Z = 8$ and neutron number $N = 20$.

In the future, the multitracks 4π-geometry detector TPC is planned to be used for the systematic study of cluster decays of the Li, Be, B, and O neutron-rich isotopes.

3.4. Search and Studying of the ^{26}O and ^{28}O Resonances Structure in Exchange Reaction. Numerous attempts [51–55] that were done with the aim of synthesizing neutron-rich oxygen nuclei ^{26}O and ^{28}O with magic number $Z = 8$ and neutron numbers $N = 18$ and 20 in fragmentation and exchange reactions in the experiments with the utmost sensitivity prove their nuclear instability. The results of these investigations have demonstrated that the nuclear drip-line structure for oxygen terminates with the last isotope having $N = 16$ neutrons (isotope ^{24}O) rather than with magic number $N = 20$. At the same time, the neutron-rich isotopes of the adjacent element fluorine with $Z = 9$ are nuclear stable with a considerably higher neutron excess $N = 22$. In order to understand the observed cause for the violation of the standard shell model predictions, it would be necessary to study the variations in the oxygen isotopes $^{20-24}$O bound states with an increase of the neutron excess, including also the search for resonances in ^{26}O and ^{28}O nuclei.

For population of the bound and unbound states of the heavy oxygen isotopes, the reactions of free one-proton knock-out from ^{27}F, ^{29}F fluorine projectile nuclei or two protons from neon ^{28}Ne, ^{30}Ne projectile nuclei can be effective [54–58]. For these goals we propose to use the fragmentation reactions of ^{36}S, ^{40}Ar, and ^{48}Ca with the energies of 40–50 MeV/A on the beryllium target nuclei (Table 4) to obtain radioactive nuclear beams of ^{27}F, ^{29}F, ^{28}Ne, and ^{30}Ne.

Table 4. **Expected production rates pps (particles per second) of heavy fluorine and oxygen isotopes (PLF) at the fragment-separator COMBAS induced in reactions of ^{36}S, ^{40}Ar, and ^{48}Ca 40 MeV/A projectiles with 200 mg/cm^2 Be target. The primary beam intensities are proposed 10 $e\mu A$**

PLF	^{36}S projectile, pps	^{40}Ar projectile, pps	^{48}Ca projectile, pps
^{25}F	$7 \cdot 10^4$	10^4	10^5
^{27}F	500	100	1000
^{29}F	2	0,2	10
^{24}O	700	200	2000
^{26}O	5	1	10
^{28}O	10^{-4}	10^{-3}	0.1

Table 5. **Estimated cross sections for stripping of a single proton and n-neutrons from nuclei of secondary fluorine beams in the energy range of the bombarding fluorine particles of 40–50 MeV/A**

X	(^{24}F, X), mb	(^{25}F, X), mb	(^{26}F, X), mb
^{24}O		3.8 ± 0.6	4.1 ± 1.4
^{23}O	6.6 ± 1.0	6.4 ± 0.9	8.9 ± 2.4
^{22}O	11.6 ± 1.6	13.1 ± 1.5	12.4 ± 2.9
^{21}O	15.1 ± 1.7	13.0 ± 1.4	13.1 ± 3.0
^{20}O	13.0 ± 1.9	8.9 ± 1.3	9.4 ± 2.2

Separation and formation of the secondary beams of radioactive ^{27}F, ^{29}F, ^{28}Ne, and ^{30}Ne nuclei will be performed on the COMBAS kinematic separator. The momentum acceptance of the separator containing the Al degrader at intermediate focus F_d must not exceed 2%. The trajectory analysis of the secondary ^{27}F, ^{29}F, ^{28}Ne, and ^{30}Ne beams (ahead of the second target) is carried out by a tracking detector which is necessary to determine the angular divergence and the size of the beam on the ^{12}C target at focus F_{a2} (Fig. 2). The isotopic identification over A and Z of the secondary radioactive nuclear beams transported to the carbon target position is unambiguously determined by time of flight (TOF) measured by the start signals from the ΔE penetrating detector 100 μm thick at focus F_{a1} and the stop signal from RF signal of cyclotron. A 100 μg/cm^2 carbon target (or a 1 mm thick polyethylene foil) at focus F_{a2} is placed ahead of the measuring detector telescope. The telescope consists [58] of a silicon ΔE penetrating detector 100 μm thick (32 strips, X coordinate) and a silicon E detector 300 μm thick (32 strips, Y coordinate). Products of proton stripping from ^{27}F and ^{29}F nuclei (or two protons from ^{28}Ne and ^{30}Ne nuclei) are identified by the combination of (ΔE, E) detector signals by the telescope and TOF using two-dimensional plots. Table 5 presents the expected cross sections of proton stripping reactions from fluorine beam nuclei ^{24}F, ^{25}F, and ^{26}F at energies of these bombarding particles of 40–50 MeV/A.

4. FUTURE OF DEVELOPMENT FOR THE COMBAS EXPERIMENTAL FACILITY

It is known [1–7] that an in-flight separating technique would not provide the unambiguous separation of reaction products over Z and A, as well as the production of monochromatic radioactive nuclear beams because of the next reasons:

i) wide range of isotopic compositions with different atomic numbers Z and mass numbers A, as well as their ions in different charge states, are created in nucleus–nucleus reactions at intermediate energies;

ii) in addition, reaction products are produced with wide momentum distributions.

The most promising method capable of solving all these problems at once implies integration of the in-flight separation with the ion catcher technique and subsequent post-acceleration towards desired energies [59, 60].

Extremely high results have been attained in recent years both in the efficiency of singly charged ion beam production (about 40–50%) and in the speed of beam extraction (several tens of milliseconds). It is planned to upgrade an experimental facility by using integration of the high-luminosity COMBAS fragment separator [7] and a fast high-efficiency ion catcher [59].

This combined facility permits one to perform the following tasks:

i) obtaining atomic beams of radioactive nuclei with the maximum intensity for subsequent acceleration;

ii) obtaining single-isotope and monochromatic beams of radioactive nuclei in a wide range of atomic numbers Z and mass numbers A;

iii) studying the mechanisms of nuclear reactions with the single-isotope and monochromatic beams of radioactive nuclei, including fusion reactions for neutron-rich isotopes of heavy and superheavy elements;

iv) studying the structure of neutron- and proton-rich isotopes of light and medium elements.

The ion catcher structure (Fig. 25) can be schematically presented as the following functional parts:

a) section for forming, diagnosing, and preliminarily slowing down (by the ΔE detector) the secondary beam of radioactive nuclei;

b) section for thermalizing radioactive nuclei in a helium-filled cell and obtaining singly charged ions;

c) section for evacuating He, extracting singly charged ions from the gas volume after their acceleration to several tens of kilovolts in the cascade of cells

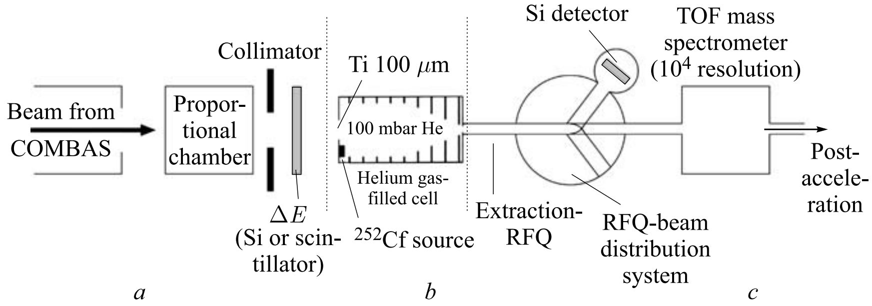

Fig. 25. Diagram of interfacing of the COMBAS separator with the ion catcher: *a*) section for forming, diagnostics, and preliminary slowing down (by the silicon ΔE detector or a scintillator) of the secondary radioactive nuclear beam; *b*) section for thermalization of radioactive nuclei in the He-filled cell and obtaining singly charged ions; *c*) section for He evacuation and for extraction of singly charged ions accelerated to energies of tens of keV in the cell of radio frequency quadrupoles (RFQ)

of radio-frequency quadrupole (RFQ), separating them from molecular impurities, and identifying by A and Z using the high-resolution mass spectrometer. Low energy singly charged ions of reaction products selected thereby with particular Z and A values can be thereafter delivered to the accelerator for post-acceleration (e.g., the DRIBS3 system).

The main component of the ion catcher setup is a cascade of gas cells developed by the Argonne National Laboratory [59]. The cell operates at a helium pressure of ~ 100 mbar, which corresponds to $\sim 0.9-1.8$ mg/cm^2 of Al equivalent for the range of 50–100 cm. The electrostatic and radio-frequency quadrupole (RFQ) devices direct moderated and thermalized ions to the outlet hole, simultaneously repelling them from the cell walls to minimize losses. The flow of evacuated He ejects ions from the gas cells via the nozzle to the subsequent section of RFQ, where they are purified from He by evacuating it at a high rate (~ 5000 m^3/h) by a high-power oil free pump. As a result, at a pressure of 100 mbar inside the gas cell cascade and an exit hole diameter of 1.6 mm, a pressure of $\sim 10^{-2}$ mbar is set up in the reducing section of RFQ. Thereafter, ions are directed to the next RFQ section, the pressure in which is maintained at a level of $\sim 10^{-5}$ mbar. After passing the cascade of focusing RFQ sections and accelerating electrostatic devices, the ion beam completely purified from He is directed to the Si detector chamber for recognition of radioactive ions by their β decays with the monitoring purpose (to determine the loss factor), after which the beam enters the high-resolution mass spectrometer. The wide-aperture mass spectrometer with a resolution of 10^4 is used to discriminate singly charged ions from singly and doubly charged molecular impurities (mainly, water molecules and hydrocarbons). The high spectrometer resolution allows one to reliably filter singly charged ions at the final focus by their mass number. Afterward, these ions can be transmitted over the transport channel for post-acceleration to desired energies.

The main characteristics of the ion catcher are the efficiency of atomic beam production and the time of ion beam extraction. The total efficiency may be checked by comparing the counting of radioactive nuclei detected by the Si detector (or the scintillation detector) at the entrance into the gas catcher (Fig. 25, section *a*) to the number of singly charged ions detected either in the focal plane of the mass spectrometer (Fig. 25, section *c*) or the second monitoring Si detector. The rate of ion beam extraction is extremely important in investigations of the most short-lived exotic nuclei, particularly, the most promising nuclei near the nuclear drip-line. The measured time of flight between the Si detector (or the scintillator (Fig. 25, section *a*)) at the entrance into the gas catcher and the detector in the focal plane of the mass spectrometer is used as a criterion of the operation speed of the entire system for converting fast secondary beams of radioactive nuclei into secondary beams of slow singly charged ions. The atomic beam extraction time of ~ 10 ms was obtained on the relativistic radioactive nuclear beams at GSI (Darmstadt, Germany) in direct experiments at the FRS + gas catcher setup [60]. In addition, the efficiency of radioactive nuclear beam conversion into beams of singly charged ions was 40–50%.

Acknowledgements. This work was supported by Russian Foundation for Basic Research (RFBR) (projects No. 13-02-00533, grants of RFBR–Ukraine No. 08-02-90406 ukr_a and RFBR–Mongolia No. 10-02-93160).

REFERENCES

1. *Anne R. et al.* The Achromatic Spectrometer LISE at GANIL // Nucl. Instr. Meth. A. 1987. V. 257. P. 215–232.
2. *Sherrill B. M. et al.* The A1200 Projectile Fragment Separator // Nucl. Instr. Meth. B. 1991. V. 56/57. P. 1106–1110.
3. *Kubo T. et al.* The RIKEN Radioactive Beam Facility // Nucl. Instr. Meth. B. 1992. V. 70. P. 309–319.
4. *Geissel H. et al.* The GSI Projectile Fragment Separator (FRS): A Versatile Magnetic System for Relativistic Heavy Ions // Ibid. P. 286–297.
5. *Artukh A. G. et al.* The Projectile-Fragment Separator COMBAS // Proc. of the Second Intern. Conf. on Radioactive Nuclear Beams, Louvain-la-Neuve, Belgium, 1991. P. 21–26.
6. *Artukh A. G. et al.* Wide Aperture Kinematic Separator COMBAS Realized on the Strong Focusing Principle // Nucl. Instr. Meth. A. 1999. V. 426. P. 605–617.
7. *Artukh A. G. et al.* The COMBAS Fragment Separator // Instr. Exp. Tech. 2011. V. 54. P. 668–681.
8. *Sereda Yu. M. et al.* Investigation of the Fragmentation of ^{20}Ne and ^{40}Ar Ions at the COMBAS Setup // Phys. At. Nucl. 2014. V. 77, No. 7. P. 817–823.
9. *Sherrill B. M.* Radioactive Nuclear Beam Facilities Based on Projectile Fragmentation // Proc. of the Second Intern. Conf. on Radioactive Nuclear Beams, Louvain-la-Neuve, Belgium, 1991. P. 3–20.
10. *Kononenko G. A. et al.* Detection System of the COMBAS Fragment Separator // Instr. Exp. Tech. 2015. V. 58. P. 337–344.
11. *Artukh A. G. et al.* Time Projection Chamber for Experiments with Heavy Ions // J. Phys. G. 1991. V. 17. P. S477–S481.
12. *Hlinka V. G. et al.* Time Projection Chambers for Tracking and Identification of Radioactive Beams // Nucl. Instr. Meth. A. 1998. V. 419. P. 503–510.
13. *Schröder W. U., Huizinga J. R.* Damped Nuclear Reactions // Treatise on Heavy-Ion Science. V. 2 / Ed. A. Bromley. New York: Plenum, 1984. P. 113–726.
14. *Aichelin J., Bertsch G. F.* Numerical Simulation of Medium Energy Heavy-Ion Reactions // Phys. Rev. C. 1985. V. 31. P. 1730–1738.

15. *Bertsch G. F., Das Gupta S.* A Guide to Microscopic Models for Intermediate Energy Heavy-Ion Collisions // Phys. Rep. 1988. V. 160. P. 189–233.

16. *Tassan-Got L., Stephan C.* Deep Inelastic Transfers: A Way to Dissipate Energy and Angular Momentum for Reactions in the Fermi Energy Domain // Nucl. Phys. A. 1991. V. 524. P. 121–140.

17. *Fuchs H., Moehring K.* Heavy-Ion Breakup Processes in the Fermi Energy Range // Rep. Prog. Phys. 1994. V. 57. P. 231–324.

18. *Artukh A. G. et al.* Forward-Angle Yields of $2 < Z < 11$ Isotopes in the Reaction of ^{18}O (35 MeV/A) with Be // Phys. At. Nucl. 2002. V. 65, No. 3. P. 393–399.

19. *Artukh A. G. et al.* Some Regularities in the Beam-Direct Production of Isotopes with $2 < Z < 11$ Induced in Reactions of ^{18}O (35 MeV/A) with Be and Ta // Nucl. Phys. A. 2002. V. 701. P. 96–99.

20. *Artukh A. G. et al.* Forward-Angle Yields of Isotopes with $3 \leqslant Z \leqslant 10$ in the Reaction of ^{22}Ne (40 MeV/A) with Be // Proc. of Intern. Symp. on Exotic Nuclei, Lake Baikal, Russia, 2001. P. 269–276.

21. *Goldhaber A. S.* Statistical Model of Fragmentation Processes // Phys. Lett. B. 1974. V. 53. P. 306–308.

22. *Aichelin J.* “Quantum” Molecular Dynamics — Dynamical Microscopic N-Body Approach to Investigate Fragment Formation and the Nuclear Equation of State in Heavy-Ion Collisions // Phys. Rep. 1991. V. 202. P. 233–360.

23. *Boal D. H., Glosli J. N.* Computational Model for Nuclear Reaction Studies: Quasiparticle Dynamics // Phys. Rev. C. 1988. V. 38. P. 2621–2629.

24. *Lukasik J., Majka Z.* CHIMERA — Microscopic Approach to Heavy-Ion Collisions at Intermediate Energies // Acta Phys. Polon. B. 1993. V. 24, No. 12. P. 1959–1980.

25. *Artukh A. G. et al.* QMD Approach in Description of the $^{18}\mathrm{O} + {}^{9}\mathrm{Be}$ and $^{18}\mathrm{O} + {}^{181}\mathrm{Ta}$ Reactions at $E_{\mathrm{proj}} = 35$ MeV/A // Acta Phys. Polon. B. 2006. V. 37, No. 6. P. 1875–1892.

26. *Artukh A. G. et al.* On the Mechanism of Forward Emitted Fragment Production in $^{22}\mathrm{Ne} + {}^{9}\mathrm{Be}$ Reaction in the Vicinity of the Fermi Energy // Acta Phys. Polon. B. 2009. V. 40, No. 1. P. 153–163.

27. *Mikhailova T. I. et al.* Asymmetry of Velocity Distributions in Peripheral Reactions with Heavy Ions at Fermi Energy // Bull. Russ. Acad. Sci. Phys. 2009. V. 73, No. 6. P. 898–903.

28. *Mikhailova T. I. et al.* Fragment Production in Peripheral Heavy-Ion Collisions at Fermi Energy in Transport Models // Intern. J. Mod. Phys. E. 2010. V. 19, No. 4. P. 678–684.

29. *Bondorf J. P. et al.* Statistical Multifragmentation of Nuclei // Phys. Rep. 1995. V. 257. P. 134–221.

30. *Morrissey D. J.* Systematics of Momentum Distributions from Reactions with Relativistic Ions // Phys. Rev. C. 1989. V. 39. P. 460–470.

31. *Blank B. et al.* Production Cross Sections and the Particle Stability of Proton-Rich Nuclei from ^{58}Ni Fragmentation // Phys. Rev. C. 1994. V. 50. P. 2398–2407.

32. *Tsang M. B. et al.* Isoscaling in Statistical Models // Phys. Rev. C. 2001. V. 64. P. 054615-1–054615-8.

33. *Mocko M. et al.* Transport Model Simulations of Projectile Fragmentation Reactions at 140 MeV/Nucleon // Phys. Rev. C. 2008. V. 78. P. 024612-1–024612-12.

34. *Bruandet J. F.* Direct Measurements of Total Reaction Cross Sections between Heavy Ions from 10 to 100 MeV/A // J. Phys. 1986. V. 47. P. 4–125.

35. *Kox S. et al.* Trend of Total Reaction Cross Sections for Heavy-Ion Collisions in the Intermediate Energy Range // Phys. Rev. C. 1987. V. 35. P. 1678–1691.

36. *Ozawa A., Suzuki T., Tanihata I.* Nuclear Size and Related Topics // Nucl. Phys. A. 2001. V. 693. P. 32–62.

37. *Knyazkov O. M., Kukhtina I. N., Fayans S. A.* Interaction Cross Section and Structure of Light Exotic Nuclei // Phys. Part. Nucl. 1999. V. 30, No. 4. P. 369–399.

38. *Erdemchimeg B. et al.* Measurements of the Total Reaction Cross Sections for ^{6,8}He and ^{8,9}Li Nuclei with Energies of 25–45 MeV/A on $^{\rm nat}$Al, $^{\rm nat}$Ta, and $^{\rm nat}$Pb // Proc. of Intern. Symp. on Exotic Nuclei, Kaliningrad, Russia, 2014. P. 148–154.

39. *Chung W., Widenthal B. H.* Collapse of the Conventional Shell-Model Ordering in the Very-Neutron-Rich Isotopes of Na and Mg // Phys. Rev. C. 1980. V. 22. P. 2260–2262.

40. *Roussel-Chomaz P. et al.* ^{16}O Elastic Scattering at $E_{\rm lab} = 94$ MeV/Nucleon // Nucl. Phys. A. 1998. V. 477. P. 345–364.

41. *Liatard E. et al.* Matter Distribution in Neutron-Rich Light Nuclei and Total Reaction Cross Section // Eur. Phys. Lett. 1990. V. 13, No. 5. P. 401–404.

42. *Artukh A. G. et al.* Study of Properties of Ne–Al Neutron-Rich Isotopes at and near $n = 20$ Magic Shell Using Elastic Scattering in Inverse Kinematics. JINR Preprint E7-93-74. Dubna, 1993. 12 p.

43. *Pietro A. Di. et al.* Elastic Scattering and Reaction Mechanisms of the Halo Nucleus ^{11}Be around the Coulomb Barrier // Phys. Rev. Lett. 2010. V.105. P. 022701-1–022701-5.

44. *Kanada-En'yo Y., Horiuchi H.* Neutron-Rich B Isotopes Studied with Antisymmetrized Molecular Dynamics // Phys. Rev. C. 1995. V. 52. P. 647–664.

45. *Ikeda K., Takigawa H., Horiuchi H.* The Systematic Structure Change into the Molecule-Like Structures in the Self-Conjugate $4n$ Nuclei // Prog. Theor. Phys. 1968. V. 68. P. 464–475.

46. *Kanada-En'yo Y., Horiuchi H., Ono A.* Structure of Li and Be Isotopes Studied with Antisymmetrized Molecular Dynamics // Phys. Rev. C. 1995. V. 52. P. 628–646.

47. *Descouvement P.* Microscopic Study of Clustering in the ^{9,10,11}Be Isotopes // Nucl. Phys. A. 2002. V. 699. P. 463–478.

48. *Freer M. et al.* Exotic Molecular States in ^{12}Be // Phys. Rev. Lett. 1999. V. 82. P. 1383–1386.

49. *Artukh A. G. et al.* Reconstruction of the Parameters of Cluster Breakup of Light Nuclei // Instr. Exp. Tech. 2009. V. 52, No. 1. P. 13–24.

50. *Jensen A. S., Riisager K., Fedorov D. V.* Structure and Reactions of Quantum Halos // Rev. Mod. Phys. 2004. V. 76. P. 215–261.

51. *Guillemaud-Mueller D. et al.* Particle Stability of the Isotopes ^{26}O and ^{32}Ne in the Reaction 44 MeV/Nucleon $^{48}\mathrm{Ca}+\mathrm{Ta}$ // Phys. Rev. C. 1990. V. 41. P. 937–941.

52. *Fauerbach M. et al.* New Search for ^{26}O // Phys. Rev. C. 1996. V. 53. P. 647–651.

53. *Tarasov O. et al.* Search for ^{28}O and Study of Neutron-Rich Nuclei near the $N = 20$ Shell Closure // Phys. Lett. B. 1997. V. 409. P. 64–70.

54. *Sakurai H. et al.* Evidence for Particle Stability of ^{31}F and Particle Instability of ^{25}N and ^{28}O // Phys. Lett. B. 1999. V. 448. P. 180–184.

55. *Hoffman C. R. et al.* Evidence for a Doubly Magic ^{24}O // Phys. Lett. B. 2009. V. 672. P. 17–21.

56. *Thoennessen M. et al.* Single-Proton Knockout Reactions from ^{24,25,26}F // Phys. Rev. C. 2003. V. 68. P. 044318-1–044318-5.

57. *Bazin D. et al.* New Direct Reaction: Two-Proton Knockout from Neutron-Rich Nuclei // Phys. Rev. Lett. 2003. V. 91. P. 012501-1–012501-4.

58. *Artukh A. G. et al.* Detecting System for Correlation Experiments in Inverse Kinematics // Proc. of Intern. Symp. on Exotic Nuclei, Lake Baikal, Russia, 2001. P. 682–689.

59. *Savard G. et al.* Development and Operation of Gas Catchers to Thermalize Fusion–Evaporation and Fragmentation Products // Nucl. Instr. Meth. B. 2003. V. 204. P. 582–586.

60. *Petrick M. et al.* Online Test of the FRS Ion Catcher at GSI // Nucl. Instr. Meth. B. 2008. V. 266. P. 4493–4497.